

# Mechanisms governing sea surface temperature anomalies in the eastern tropical Pacific Ocean associated with the boreal winter Madden-Julian Oscillation

Lisanne E. Lucas,<sup>1,2</sup> Duane E. Waliser,<sup>3</sup> and Raghu Murtugudde<sup>4</sup>

Received 28 April 2009; revised 30 September 2009; accepted 2 November 2009; published 13 May 2010.

[1] The study objective is to explore the relationship between the Madden-Julian Oscillation (MJO) and intraseasonal sea surface temperature (SST) variability in the eastern tropical Pacific Ocean. Previous studies have illustrated the connection between MJO and the production of zonally large (>2000 km), persistent (~weeks) SST anomalies. Those studies suggested that vertical processes, such as advection and entrainment, forced remotely by winds in the western Pacific (via Kelvin waves) may be the mechanism controlling SST changes. To overcome limitations in situ observations (e.g., sparse and missing data/quantities) and to develop a more comprehensive physical understanding, this study examines the relationship using an ocean general circulation model. A simulation was conducted in which the model was forced by idealized MJO conditions constructed from observed forcing fields. Analysis of the model simulation shows an equatorial Kelvin wave initiated in the western Pacific Ocean. However, analysis of the model's mixed layer temperature heat budget shows that in the eastern Pacific meridional advection plays the major role in the sea surface temperature change, 61.8% of the warming phase and 70.7% of the cooling phase percent heat budget. Zonal advection is the second most important term to the warming phase (20.5%) with the vertical advection and mixing term being second for the cooling phase (37.6%). In addition, the results indicate that the primary component of the meridional advection is the advection of the mean meridional temperature gradient by MJO-forced meridional current anomalies. The implications and caveats of these results are discussed in relationship to results in prior studies.

**Citation:** Lucas, L. E., D. E. Waliser, and R. Murtugudde (2010), Mechanisms governing sea surface temperature anomalies in the eastern tropical Pacific Ocean associated with the boreal winter Madden-Julian Oscillation, *J. Geophys. Res.*, 115, C05012, doi:10.1029/2009JC005450.

## 1. Introduction and Background

[2] The Madden Julian Oscillation (MJO) is the dominant feature of atmospheric variability in the Tropics at the intraseasonal (35–95 days) time scale. MJOs are characterized by large-scale eastward propagating fields of strong zonal wind anomalies and complex convective patterns which exhibit strong cloud and rainfall anomalies [Madden and Julian, 1971, 1994]. The convection anomaly for a typical MJO will begin in the equatorial Indian Ocean and propagate eastward to the western and central Pacific Oceans. The

MJO can play an important role in air-sea interaction via wind effects on surface latent heat flux and momentum transfer, and cloud effects on surface shortwave radiation. During the northern hemisphere wintertime the MJO convection anomaly remains roughly symmetrical about the equator and slightly south; during summertime the convection anomaly tends to shift northward [Wang and Rui, 1990; Waliser, 2006].

[3] The MJO is known to have extensive influence on a number of climate and weather phenomena in and beyond the tropical atmosphere such as, the active and break periods of the Asian monsoon [Yasunari, 1979; Lau and Chen, 1986; Lawrence and Webster, 2001], genesis of tropical cyclones in the Pacific Ocean and the Caribbean [Liebmann *et al.*, 1994; Higgins and Shi, 2001], variability in rainfall along the west coast of North America [Jones, 2000], South America [Liebmann *et al.*, 2004] and Africa [Matthews, 2004], and oceanic and atmospheric composition [Tian *et al.*, 2008].

[4] It can be seen in observational evidence that westerly wind events associated with MJO can likely influence

<sup>1</sup>Institute for Terrestrial and Planetary Atmospheres, State University of New York at Stony Brook, Stony Brook, New York, USA.

<sup>2</sup>Now at Climate Program Office, NOAA, Silver Spring, Maryland, USA.

<sup>3</sup>Water and Carbon Cycles Group, Jet Propulsion Laboratory, Pasadena, California, USA.

<sup>4</sup>Earth System Science Interdisciplinary Center, University of Maryland, College Park, Maryland, USA.

ocean variability in the eastern Pacific, an area vital to the development of El Niño–Southern Oscillation (ENSO). The rapid development of the El Niño in 1997 was significantly influenced by higher-frequency variability such as MJO [McPhaden, 1999]. The time period leading up to the onset of El Niño (late November 1996 to May 1997) was characterized by increasingly strong MJO zonal wind activity in the western Pacific. This was followed approximately two months later by rapid warming of sea surface temperature (SST) in the eastern Pacific (February–August). Weickmann [1991] demonstrated that there may be a potential relationship between strong MJO events and the triggering of the onset of the 1981–1982 El Niño. He examined outgoing longwave radiation (OLR), 150 mbar atmospheric circulation patterns, and SST anomalies for the time period of September 1981 to April 1982. This period covered the transition phase to El Niño conditions and included 6 MJO events. He found that the passage of strong MJOs from the Indian Ocean to the Pacific can influence the interannual anomalous atmospheric circulation and the SST anomalies in the western and central Pacific during the onset period of ENSO development.

[5] Kessler *et al.* [1995] used moored ocean buoys from the Tropical Atmosphere–Ocean (TAO) array along the equator to examine the relationship between wind stress, 20°C isotherm depth and SST. They found that the wind stress anomalies associated with MJO can produce intraseasonal Kelvin waves that travel across the Pacific and account for a major component of the eastern Pacific thermocline depth variability. These Kelvin waves travel at a speed of 2.4 m/s and have a large zonal structure ( $>10,000$  km or  $90^\circ$  of longitude). Hendon *et al.* [1998] expanded on and confirmed the Kessler *et al.* study by using the TAO 20°C isotherm depth, ECMWF vector winds, and OLR. They used a statistical empirical orthogonal function analysis (EOF) method to isolate intraseasonal Kelvin wave signals in the 20°C isotherm depth. They found that intraseasonal Kelvin waves have an eastward phase speed of 2.3 m/s and a west to east travel time across the Pacific basin of approximately 70 days. They also state that intraseasonal Kelvin waves are predominantly forced by eastward moving wind stress anomalies west of  $170^\circ\text{W}$  produced by the MJO.

[6] It has since been suggested by Zhang [2001] that intraseasonal SST variations observed in the equatorial eastern Pacific could be related to the MJO via the above described ocean Kelvin wave activity. The intraseasonal SST perturbations that Zhang describes appear as a large, coherent anomaly (zonal scale of 2000–5000 km; meridional scale of  $\sim 500$  km) straddling the equator and reaching from approximately  $90^\circ\text{W}$  to  $130^\circ\text{W}$ . These intraseasonal SST perturbations should not be confused with SST anomalies often associated with tropical instability waves (TIW) that are found near the mean SST front north of the equator. SST anomalies associated with TIWs have a period of 20–40 days and a smaller spatial scale of 800–2000 km [e.g., Pullen *et al.*, 1987]. Zhang hypothesized that strong MJO westerly (or easterly) winds in the western/central Pacific initiate downwelling (upwelling) Kelvin waves that travel eastward. These downwelling (upwelling) Kelvin waves depress (lift) the thermocline in the eastern Pacific, which is normally shallow due to upwelling, thus altering the vertical advection and temperature gradient. The normal cooling effect of the

upwelling is suppressed (enhanced), and as a result the SST warms (cools). Zhang developed this hypothesis using SST and 20°C isotherm depth data from the TAO buoy array, Reynolds and Smith's [1994] weekly SST data and wind data from European Remote Sensing satellites [Bentamy *et al.* 1996]. He found that fluctuations in the intraseasonal vertical advection in the eastern Pacific varied coherently with the intraseasonal eastern Pacific SST perturbations on interannual time scales.

[7] McPhaden [2002] also used the equatorial portion of the TAO buoy array to examine intraseasonally varying sea surface temperatures in the Pacific. His study focused on documenting the processes affecting SST variability at four sites along the equator: the western Pacific warm pool ( $165^\circ\text{E}$ ), the eastern Pacific cold tongue ( $110^\circ$  and  $140^\circ\text{W}$ ), and a central transition zone ( $170^\circ\text{W}$ ). Using a mixed layer heat balance approach he analyzed the relative contribution of surface heat flux, horizontal advection, and a combined term called “vertical advection and entrainment.” The vertical advection term could not be directly measured but was derived from an estimated vertical velocity composed of the difference between the time variations in the 20° isotherm and the mixed layer depth ( $W'$ ), and a mean vertical velocity ( $W_{\text{bar}}$ ) based on shipboard ADCP measurements. McPhaden found that vertical advection and entrainment were the dominant processes in the eastern Pacific. Further, he went on to note that Kelvin waves strongly mediate the dynamical processes that control the SST variability in that region. Additionally, he found that local surface heat fluxes can influence these dynamically induced SST variations and tends to damp them at a rate of about  $20\text{ W m}^{-2}\text{ C}^{-1}$ .

[8] However, examining the results of McPhaden [2002] or the Zhang [2001] hypothesis by using observational evidence alone could give a misleading conclusion due to the inability of the ocean observations to capture the full nature of this dynamical system. For example, the Zhang study focuses on linking Kelvin wave activity to SST changes by relating fluctuations in the vertical temperature gradient with Kelvin wave activity. However, the meridional and zonal advection, potentially important terms in the eastern Pacific mixed layer heat budget, are not included in his analysis. For the McPhaden study period of 1991 to 1999, the TAO buoy array recorded current data (i.e.,  $U$ ,  $V$ ) only on buoys located along the equator at  $165^\circ\text{E}$ ,  $170^\circ\text{W}$ ,  $140^\circ\text{W}$ , and  $110^\circ\text{W}$ . McPhaden's approach relied on analyzing horizontal and vertical advection terms for the surface mixed layer. However, the current meter and ADCP data he used contains temporal gaps in the surface layer (0–50 m) that ranged from weeks to several months most importantly during the lead up to the 1998 El Niño. Also, his application does provide for the analysis of the horizontal advection terms at these select locations but it does not allow for the analysis of meridional advection at potentially important off equatorial regions such as  $2^\circ\text{N}$  and  $2^\circ\text{S}$  where, in the eastern basin, there are large mean meridional temperature gradients. Given the very strong gradients in both dynamic and thermodynamic properties in the near-equatorial region, and the possibility that vertical and larger-scale meridional processes are important, it is crucial to be able to better quantify all components of the surface heat budget in the entire region associated with the intraseasonal SST anomalies (i.e.,  $\sim 5^\circ\text{N}$ – $5^\circ\text{S}$ ).

[9] In an alternative approach, *Waliser et al.* [2003] used the *Gent and Cane* [1989] ocean general circulation model (OGCM) to ascertain the basin-wide impact of composite MJO forcing on the near-surface ocean. They found a SST signal very similar to that observed by Zhang. Their preliminary analysis of the ocean heat budget in the eastern Pacific suggests that horizontal advective processes may play a significant role in the formation of the anomalous SSTs. More specifically, they found that the meridional advection term was a principal contributor to the intraseasonal warming and cooling events forced by the MJO.

[10] The purpose of this study is to explore the equatorial eastern Pacific Ocean's response to idealized MJO forcing. Specifically, this study will focus on describing the ocean dynamics and air-sea exchange processes associated with intraseasonal SST anomalies. To adequately answer this question it is necessary to use high-quality atmospheric forcing data and a numerical model that is robust in simulating ocean variability at relevant time scales: seasonal, interannual and in particular intraseasonal. It is equally important to make comparisons of the ocean model results to ocean observations as a way to measure the fidelity of the model experiment.

[11] This study expands on the *Zhang* [2001], *McPhaden* [2002], and *Waliser et al.* [2003] results mentioned above, and diagnoses the main mechanisms that are affecting intraseasonal SSTs in the equatorial eastern Pacific. In this study, the *Gent and Cane* OGCM, similar to that discussed by *Waliser et al.* [2003], is used to examine the dynamics and thermodynamics that induce these SST variations. In section 2, the OGCM is described in detail, and the experimental setup and forcing scenarios that are used to diagnose the dominant mechanisms controlling the SST variations are discussed. In section 3, results from a model validation study and the idealized MJO study will be presented. Section 4 gives a comprehensive summary and discussion of the results in the context of observational data and previous studies.

## 2. Description of the OGCM Model, Data, and Setup

### 2.1. OGCM Description

[12] The *Gent and Cane* [1989] ocean model is a reduced gravity, primitive equation model in sigma coordinates. The model uses 25 sigma layers in the vertical including a mixed layer; the last sigma layer resides above a quiescent plane [*Murtugudde et al.*, 1996]. The thickness of the mixed layer and the lowest layer are calculated prognostically at each grid point. The thickness of the intermediary layers, between the mixed layer and the lowest layer, are determined such that the ratio of each sigma layer to the total depth below the mixed layer is held to a specified fraction. This is comparable to a modified pressure coordinate system and creates a flexible vertical model structure that allows the layer thicknesses to vary from grid point to grid point. Second-order central differences are used to calculate the vertical components of the model. The horizontal structure of the model uses an "A" grid [*Arakawa and Lamb*, 1977]. The domain boundaries are 30°N to 30°S and from 32°E to 76°W. The spatial resolution is 1/3° latitude by 1/2° longitude. Fourth-order central differences are used to calculate the

horizontal advection. Horizontal friction is addressed by using a high-order, scale-selective *Shapiro* [1970] filter. For time integration, the Lorenz N cycle scheme is used [*Lorenz*, 1971]. The model is forced using daily values and uses a 360 day year or 72 pentad year.

[13] The model mixed layer uses the *Chen et al.* [1994] hybrid mixing scheme to interact with the atmospheric boundary layer above and the thermocline below. This scheme is preferable as it combines the traditional bulk mixed layer model of *Kraus and Turner* [1967] and the dynamic instability model of *Price et al.* [1986]. This accounts for the three major turbulent mixing processes: mixed layer entrainment/detrainment due to atmospheric wind stirring and heat flux (bulk mixed layer model), shear flow instability (based on the gradient Richardson number), and an instantaneous adjustment for high-frequency convection in the thermocline (dynamic instability model). Complete freshwater hydrology is included in the model [*Murtugudde and Busalacchi*, 1998] as a surface boundary condition. The model set up uses a sponge layer at the north and south boundaries where salinity and SST values are damped toward the climatological values of *Levitus and Boyer* [1994].

[14] The ocean model is coupled to an advective atmospheric mixed layer model (AMLM [*Seager et al.*, 1995]). The coupled AMLM calculates the surface heat fluxes between the atmosphere and the ocean and uses them to determine the SST field for the next time step. The coupling of the OGCM to the AMLM improves the simulation of tropical SSTs and their feedbacks to model dynamics and thermodynamics [*Seager and Blumenthal*, 1994; *Murtugudde et al.* 1996]. The AMLM uses solar radiation, cloud cover and winds as external forcing fields to compute first, the boundary air temperature and humidity, and then the surface heat fluxes based on the model SST. The standard bulk formula and observed cloud cover are used to calculate the longwave radiation [*Seager and Blumenthal*, 1994]. Air temperature, humidity and imposed winds are used to calculate the surface sensible and latent heat fluxes. Note that in the proposed configuration, there is no heat flux adjustment applied to the model.

[15] A spatially varying attenuation depth for solar radiation based on the Sea-Viewing Wide Field-of-View Sensor (SeaWiFS) ocean color data set was used here to address the cold bias in the eastern Pacific that was noted by *Waliser et al.* [2003]. The vertical structure of local heating in the upper layers of the ocean is affected not only by the amount of solar radiation impinging on the surface but also by the amount of particulate matter in the water column. According to *Murtugudde et al.* [2002], an improvement in the representation of the penetrating solar radiation (via attenuation depth) can lead to improvements in the SST response in the eastern Pacific. See *Murtugudde et al.* [2002] for details on the implementation of attenuation depth scheme.

[16] In addition to the freshwater hydrology mentioned above, the model incorporates the impacts of riverine discharge to the upper ocean. For further details of the model, its setup and execution please refer to *Lucas* [2007].

### 2.2. Model Forcing Setup and Data: Climatology

[17] The required surface forcing fields for the model are precipitation, solar radiation, cloud cover, surface wind and

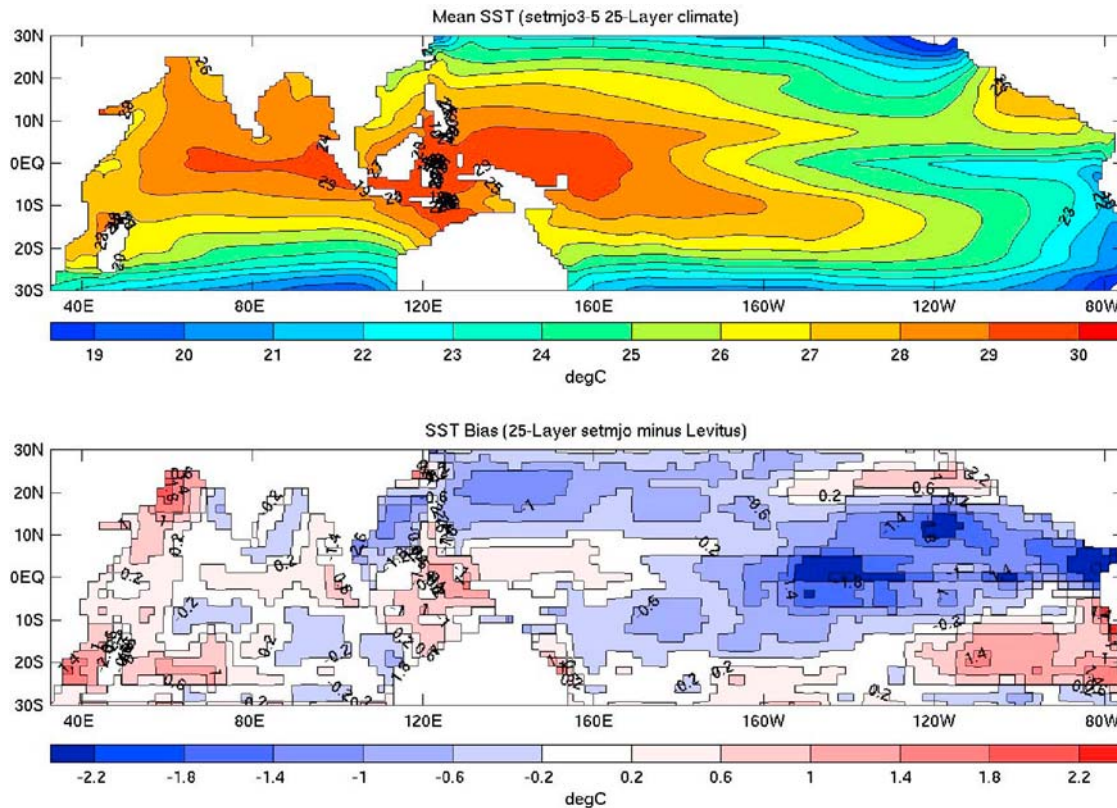


**Figure 1.** (top) Mean annual SST for the model. (bottom) Mean annual bias in SST for the model based on *Levitus and Boyer's* [1994] observed SST.

stress, and at the continental margins, the surface wind, the air temperature, and air humidity. For the spin-up and the climatology runs, the model was forced with daily averages from the annual cycle of precipitation from the *Xie and Arkin* [1997] data set, ISCCP C “total cloud fraction” [Rossow and Schiffer, 1991], and shortwave radiation from Earth Radiation Budget Experiment (ERBEE [Li and Leighton, 1993]). The precipitation data from Xie and Arkin is a blended product of in situ and satellite data. The data used for the climatological values of air temperature and humidity at the continental margins were obtained from European Centre for Medium-Range Weather Forecasts (ECMWF) ERA-15 reanalysis product.

[18] The surface wind data used for the wind and wind stress calculation are from the Special Sensor Microwave/Imager (SSM/I) [Atlas *et al.*, 1996]. SSM/I winds are a satellite derived ocean wind speed (at 10 m) data product. The wind data was processed from daily values of zonal and meridional wind from 1988 to 1999 to daily values of wind stress, direction and speed. The daily values were used to compute a 365 day annual average for each quantity which were then interpolated to 12 month annual cycles. Wind stress was calculated from wind speed using the bulk aerodynamic formula:  $\vec{\tau} = \rho_{air} C_D |\vec{U}_{10}| \vec{U}_{10}$ , where air density ( $\rho_{air}$ ) was defined as  $1.25 \text{ kg/m}^3$  and the drag coefficient ( $C_D$ ) as  $1.5 \times 10^{-3}$ .

[19] An additional constraint was placed on the climatological winds produced from SSM/I winds. The wind data used for this setup are processed in a specific way as to

provide for the gustiness of the natural system that satellite measurements typically cannot account for. A gustiness factor was applied to the data such that there is a minimum wind speed threshold of 4 m/s. This threshold was applied to the climatological data, rather than incorporated into the model code, in order to allow wind values to fall below 4 m/s during periods of anomalous wind forcing such as low-wind conditions during the MJO forcing periods. This is discussed in more detail by *Waliser et al.* [2003].

[20] The climatological run was forced using annual cycle forcing from the data described above. It was initiated from climatological values of SST and salinity from the World Ocean Atlas [Levitus and Boyer, 1994] and integrated for 20 years to establish model equilibrium. The final three years of the spin-up period were averaged to establish the model climatology, the state relative to which model anomalies are calculated.

[21] The mean annual model SST is shown in Figure 1 (top). It shows a realistic annual mean SST with a western Pacific warm pool extending out to approximately 170°E and a cool eastern Pacific upwelling region extending west along the equator. Figure 1 (bottom) shows the bias of the model SST response compared to the *Levitus and Boyer* [1994] observed SST data set. The western Pacific warm pool is slightly biased warm with values ranging from ~0 to 0.3°C. There is also a stronger cold bias in the equatorial eastern Pacific with values of -0.2 to -1.4°C. The appearance of blockiness in Figure 1 (bottom) is due to the Levitus and Boyer data set being sampled on a 2° by 2° grid whereas

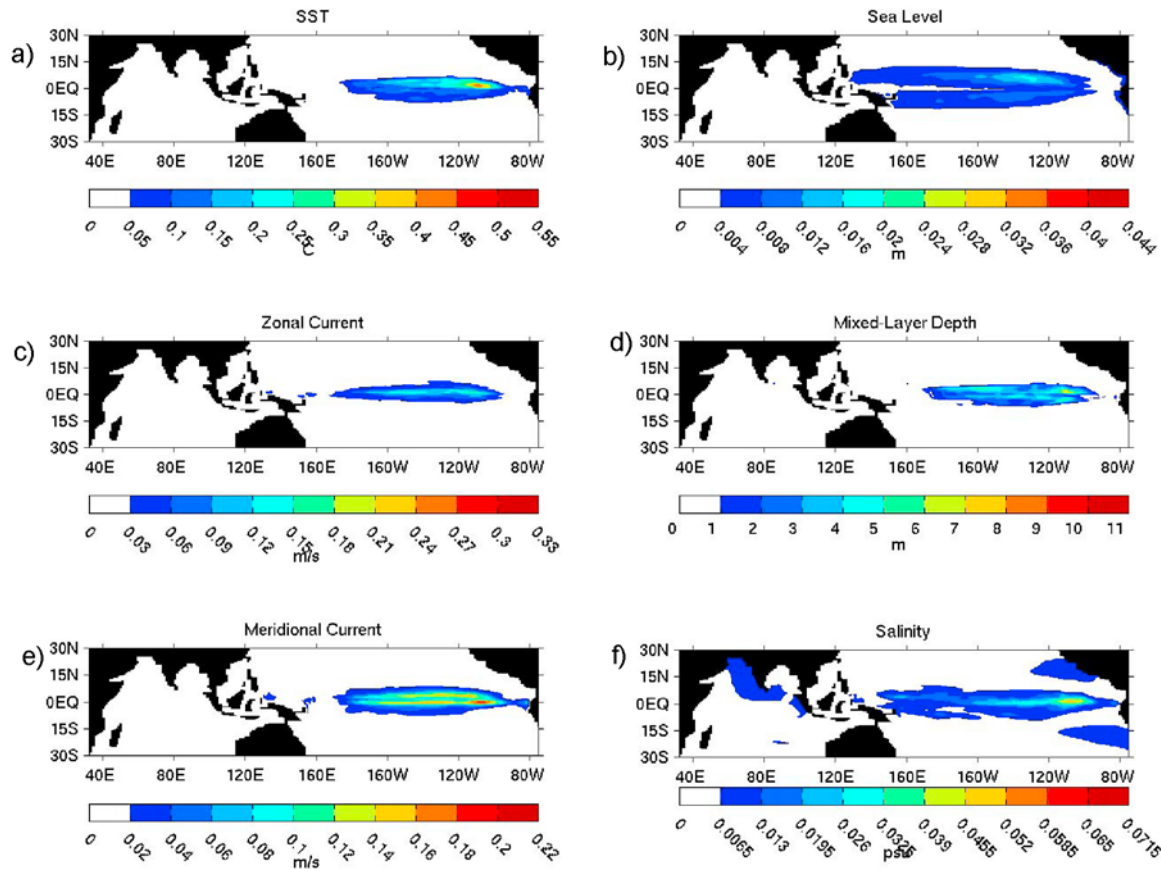


**Figure 2.** Internal variability (variance internal to the model, when forced by climatological forcing, but not associated with the annual cycle) of the model with regard to (a) SST, (b) sea level, (c) zonal current ( $U$ ), (d) mixed layer depth, (e) meridional current ( $V$ ), and (f) salinity for the full 12 month climatological year. This variance is shown in terms of standard deviations.

the model resolution is  $1/3^\circ$  by  $1/2^\circ$  grid. The model data was averaged to a  $2^\circ$  by  $2^\circ$  resolution prior to comparison with the Levitus and Boyer data set.

[22] The climatological run was also used to determine the internal variability of the model. Internal variability is that fraction of variance which is internal to the model, is non-deterministic, and is not associated with the annual cycle response. To construct the internal variability, the 3 year climatology data was averaged to form an annual cycle for each pentad at each grid point. The annual cycle was then removed from the three years of data and the mean variance was computed. Figure 2 shows the internal variability of the model with regard to SST, sea level, mixed layer depth, zonal current ( $U$ ), meridional current ( $V$ ) and salinity. This variance is shown in terms of the standard deviation. It is apparent from Figure 2 that the internal variability is almost entirely contained in the equatorial Pacific, with major sources, such as tropical instability wave activity in the SST, in the eastern Pacific region. The maximum values for SST, sea level, mixed layer depth, zonal current, meridional current and salinity are 0.4257 °C, 1.7 cm, 6.8 m, 15.8 cm/s, 18.3 cm/s and 0.049 psu. The variability in salinity due to the impact of the riverine discharge can be clearly seen in the Indian Ocean basin, west of India with a value of 0.010 psu.

### 2.3. Model Forcing Setup and Data: MJO

[23] The surface forcing fields associated with the MJO were constructed in the same manner as those described by *Waliser et al.* [2003]. The goal of the composite approach is to construct an idealized MJO pattern from observed fields that is representative of a “typical” northern hemisphere winter MJO event. With that in mind, a canonical MJO pattern was identified using an extended empirical orthogonal function (EEOF) analysis of filtered pentad (i.e., 5 day averaged) Northern Hemisphere winter rainfall data [*Xie and Arkin*, 1997] for the years 1979 to 1999. A 35–95 day Lanczos [*Duchon*, 1979] filter was applied to the full data series prior to the reduction to only winter months (winter is defined here to be November–April). The EEOF was computed for  $\pm 7$  pentad time lags on the region between  $30^\circ\text{N}$  to  $30^\circ\text{S}$ , and  $30^\circ\text{E}$  to  $180^\circ\text{E}$ . This region, which includes the Indian Ocean and western Pacific Ocean, was selected due to the strong influence that MJO has on the rain variability in that area during winter.

[24] Candidate MJO events were chosen based on the EEOF Mode 1 unit normalized amplitude time series. When the value of the amplitude time series for mode 1 exceeded 1.2 [see *Waliser et al.*, 2003, Figures 2 and 3], the band-passed data was selected such that  $\pm 7$  pentads around the peak amplitude were included. The resulting selection cap-



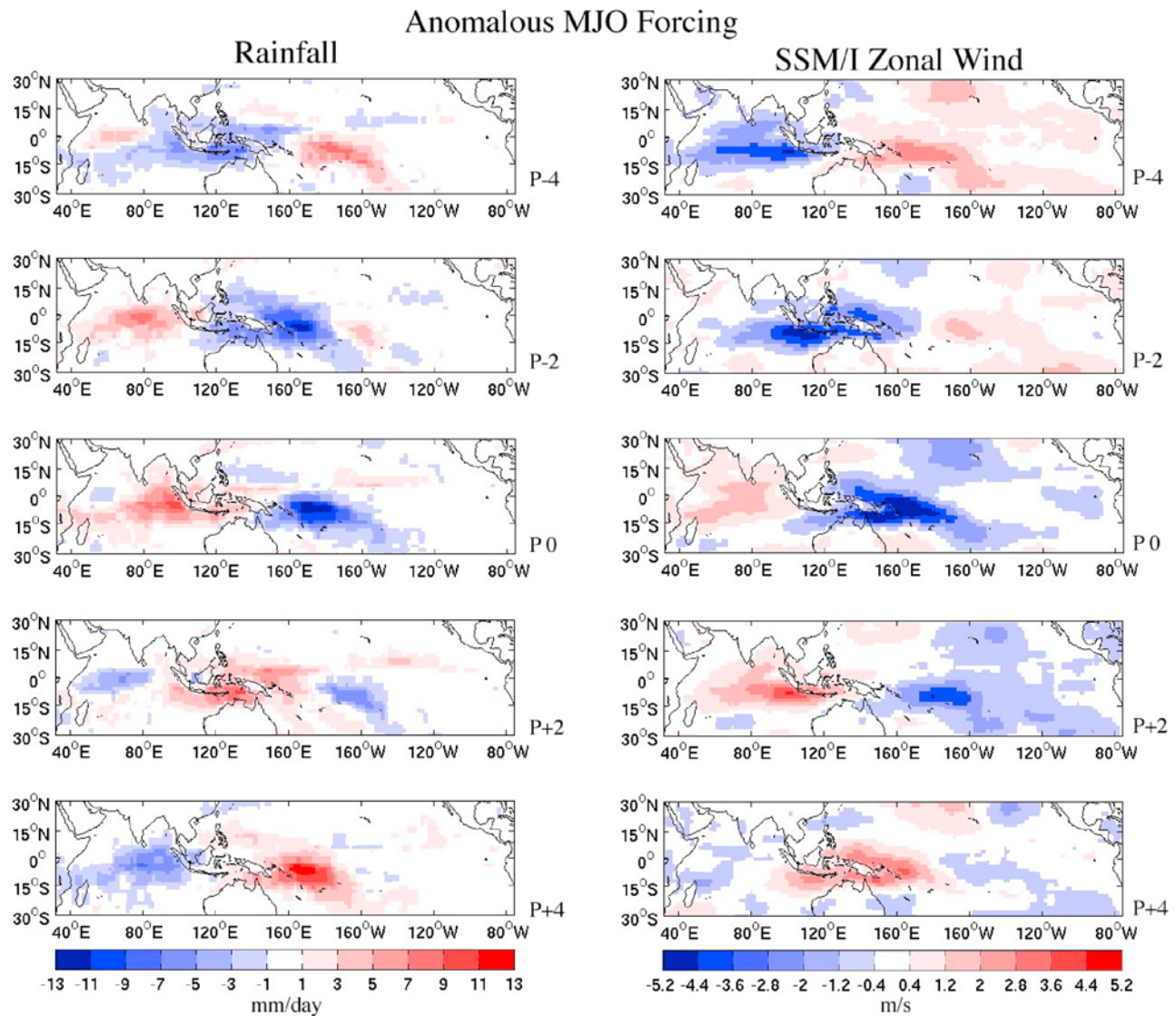


**Figure 3.** Anomalous MJO forcing for (left) rainfall and (right) zonal winds. Time progresses downward from P – 4 (Pentad lagged by –4) to P0 to P + 4 denoting the position in the forcing cycle, every 2 pentads (10 days) shown. The cycle completes and repeats in 10 pentads (50 days).

tured 31 MJO rainfall events used to produce a composite (average) forcing structure 15 pentads in length. The other surface forcing fields included: (1) shortwave obtained from daily ISCCP-derived surface shortwave values, available mid-1983 to mid-1991 [Bishop *et al.*, 1997]; (2) winds from daily SSM/I, available 1988 to 2000 [Atlas *et al.*, 1996]; and (3) cloud fraction from daily ISCCP-D-derived total cloud fraction, available mid-1982 to 2000 [Rossow and Schiffer, 1991]. However, due to the differing availability of some of the data sets, the number of selected events may be different between fields. The number of events that went in to composites for shortwave, cloud fraction and wind are 14, 19, and 19, respectively. Consistent with the previous work by Waliser *et al.* [2003], a scale multiplier of 1.7 was applied to each composite to compensate for the decrease in magnitude associated with the averaging.

[25] Using the above method, a single idealized, average wintertime (November–April) MJO event was produced for

observed fields of rain, shortwave, wind speed, wind stress, and cloud fraction. Figure 3 shows the composite MJO cycle of surface forcing for rain (Figure 3 (left)) and zonal wind (Figure 3 (right)). Each series is a 10 pentad (50 day) cycle beginning with P – 4, which exhibits an eastward propagating dipole structure that begins in the Indian Ocean and moves to the western Pacific. For example, the structure of growing positive rainfall in the Indian Ocean in P – 4 moves through to the western Pacific in P + 4 and appears again in P – 4 in western Pacific where it begins to decay through P – 2. The rainfall maximum is approximately 12 mm/d and is located over the western Pacific warm pool. Comparison of the rainfall with the zonal wind series shows easterly winds traveling ahead of the positive MJO rainfall event and westerly winds developing behind. The zonal wind maximum for easterlies is approximately 4.5 m/s and located in the western Pacific. It should be noted that due to the

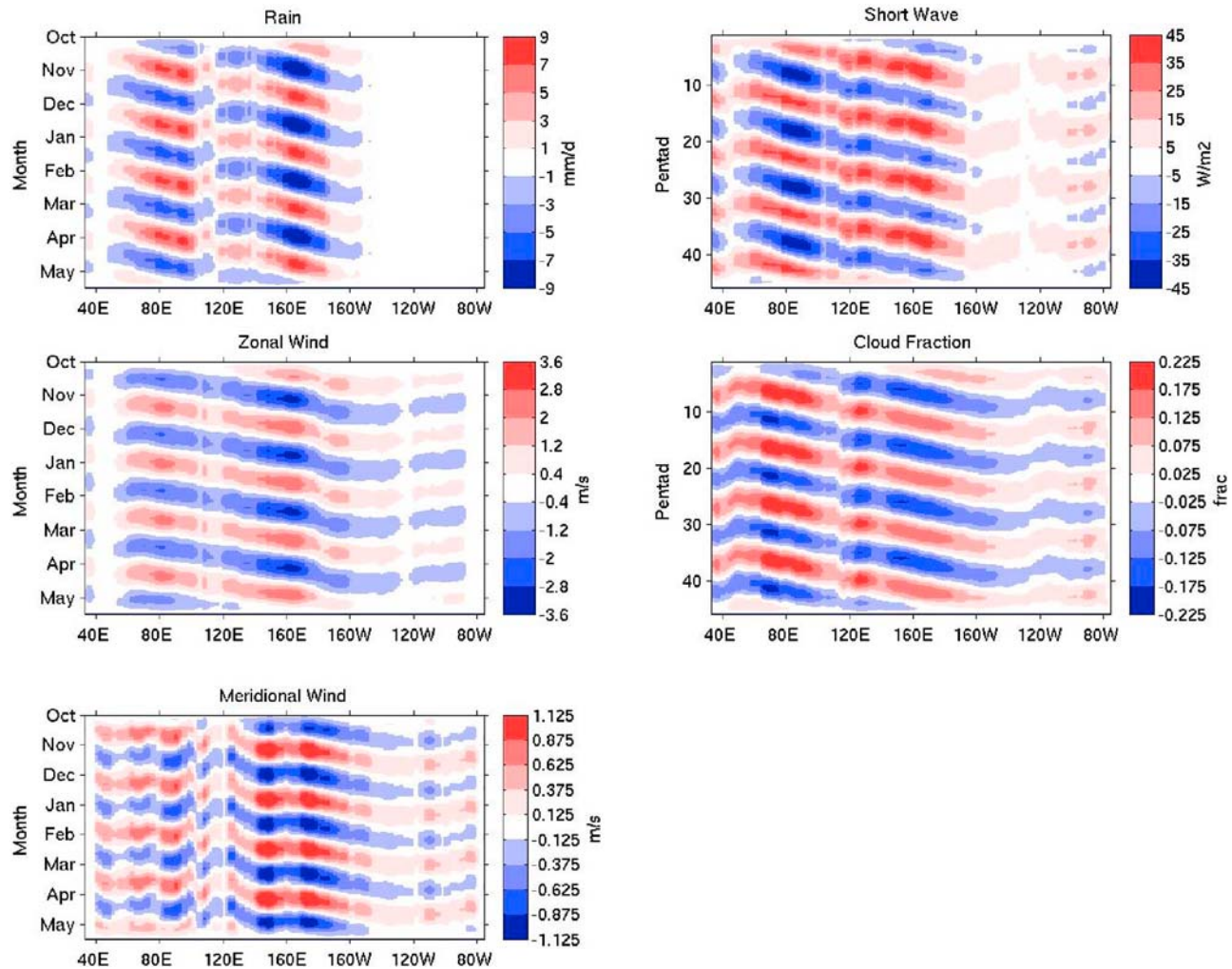


**Figure 4.** Anomalous MJO forcing averaged 3°N–7°S.

seasonality of the MJO the major part of the forcing in all fields occurs in the region of 5°N to 10°S.

[26] It can be seen in the comparison of  $P + 4$  in Figure 3 with  $P - 4$  that the cycle is repeating in nature. Since the nature of MJO is cyclic, and the MJO often has several events occurring in one season, the single idealized MJO event (10 pentads) was concatenated together four times to form a repeating series that lasts during the months of October–May. The repeating series includes four sets of 10 pentads idealized MJO events ( $P - 4$  (i.e., minus 4 lag) through  $P + 5$  (i.e., plus 5 lag, not shown)) plus 3 pentads at the beginning (and end) to build up (and taper off) the forcing. The beginning (ending) pentads are 0, 1/3, and 2/3 (2/3, 1/3 and 0) the strength of the first pentad of the composite event.

[27] To illustrate the repeating nature of the applied forcing, Figure 4 shows the series of four composite surface forcing events concatenated together for the fields of rain, zonal wind, meridional wind, shortwave and cloud fraction. The forcing shown here is equatorially averaged over latitudes of 3°N to 7°S and lasts for 46 pentads from October to May. Comparison of the zonal wind forcing to that observed by the TAO array (Tropical Atmosphere–Ocean Project [Hayes et al., 1991; McPhaden et al. 1998]) data set in the

Pacific Ocean during the period of November 1996 to May 1997 shows that the construction of MJO forcing is realistic in magnitude and frequency. It can be seen that cloud fraction forcing (and inversely, shortwave) closely follows the rainfall pattern in the Indian Ocean and western Pacific. However, the cloud fraction in the eastern Pacific shows cloud cover without MJO associated rain.

[28] The MJO forcing presented in this paper has been idealized in several ways including compositing multiple events into one event and concatenating four equally sized events into one season. Justification for this approach can be found by Waliser et al. [2003] where a comparison of cycle amplitude and number of wintertime events are made to observed wintertime MJO activity in the Pacific and Indian Oceans.

#### 2.4. Model Forcing Setup and Data: Validation and Observations

[29] For the purpose of model testing and direct comparison with observed data, the model was forced with total observed fields of rain [Xie and Arkin, 1997], SSM/I winds [Atlas et al., 1996], ISCCP C cloud fraction [Rossow and Schiffer, 1991], and ISCCP shortwave radiation [Bishop et al., 1997] from the period of 1 January 1990 to 26 June

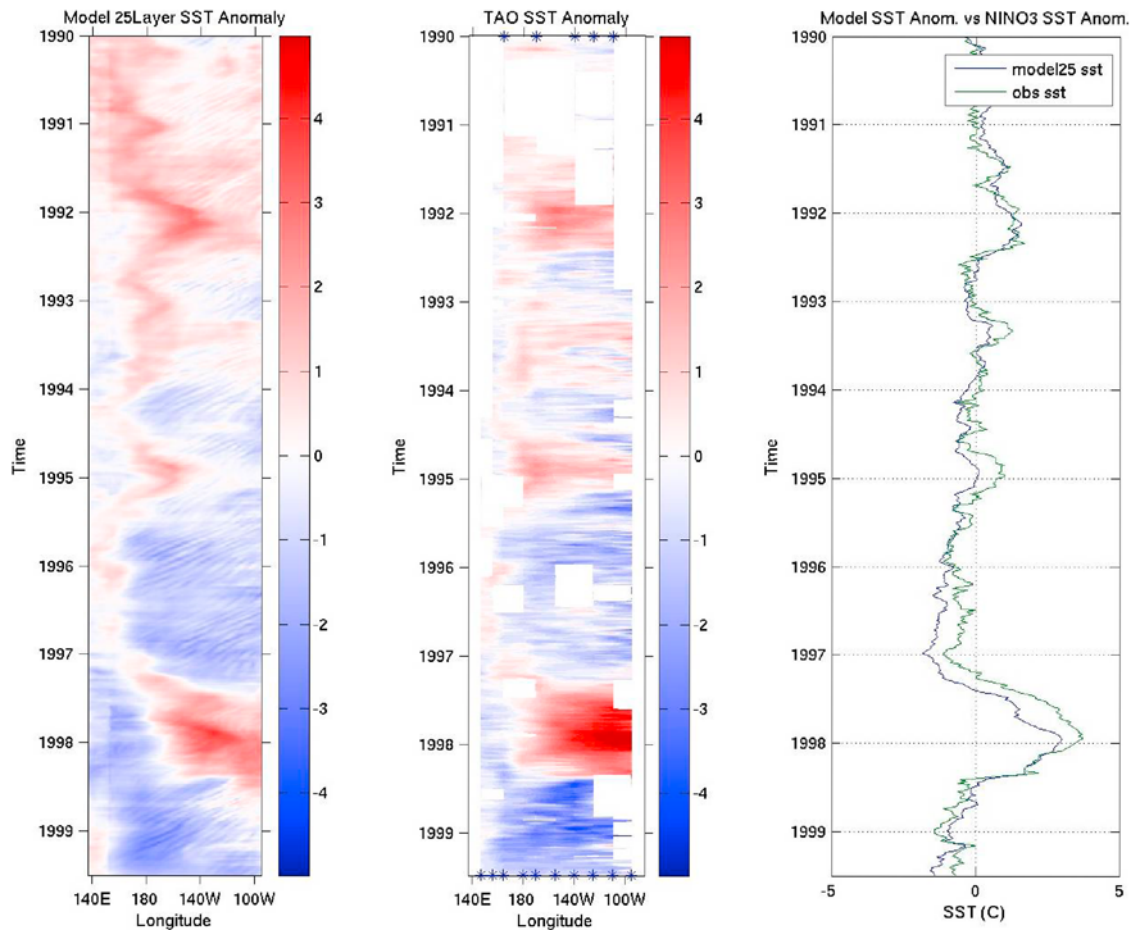


**Figure 5.** (left) Anomalous SST for the model at the equator for the years 1990 to July 1999. (middle) TAO anomalous SST data for the same period. The white regions are areas of missing data, and blue asterisks on upper (lower) axis mark buoy locations during early 1990s (mid-1990s). (right) Comparison of the model with the Nino3 SST Index.

1999. These dates were chosen to allow for comparisons with the TAO buoy data, which was used in the previously published study of Zhang [2001]. The processing of the surface forcing data for these runs was similar to the climatological forcing data. Daily values were interpolated to a 72 pentads per year basis (roughly 5 day averages).

### 3. Results

#### 3.1. Description of the OGCM Ocean Response: Validation

[30] Tests were made to the OGCM to assess the ability of the model to reproduce realistic sea surface and subsurface temperature mean conditions and variability in the equatorial eastern Pacific Ocean using the 9.5 years of observed forcing fields described in section 2.4. A 20 year spin-up period using the climatological (i.e., annual cycle) forcing conditions described section 2.2 was used to initiate the validation run.

[31] The model ocean response is compared with 9.5 years of SST data from the Tropical Atmosphere Ocean (TAO) buoy array [Hayes *et al.*, 1991; McPhaden *et al.*, 1998], Levitus SST data [Levitus and Boyer, 1994], and SST data from the Nino3 region (5°N–5°S, 150°W–90°W) of the

equatorial Pacific. The TAO buoy grid is composed of 67 buoys located on a rectangular, semiuniform grid (10–15° longitudinal, 2–3° latitudinal separation) in the equatorial Pacific covering the domain of 9°N–8°S, 137°E–95°W. It should be noted that some buoys have longer time records than others due to the addition of buoys to the array in the mid-1990s and some periods of those records have missing data due to equipment failure. Daily TAO data was averaged to 5 day pentad data after the leap days were removed. The Nino3 SST index is a weekly SST data product and is available from <http://www.cpc.noaa.gov/data/indices/>.

[32] The anomalous SST field at the equator for the 9.5 year simulation is shown in Figure 5 (left). The model data shown here has been subset to the equator in the Pacific Ocean for comparison with TAO SST data (Figure 5 (middle)). The TAO data is composed of those buoys along the equator which are noted in Figure 5 with asterisks along the abscissa. Figure 5 (right) shows a comparison of the modeled SST to observed SST in the Niño3 region (5°N–5°S, 150°W–90°W). Figure 5 (left) shows the anomalous SST response at the equator relative to the model climatology (see section 2.2 for definition) for the 9.5 year simulation. Here the 1997–1998 El Niño event is clearly seen as an anomalous warming of approximately 4°C in the eastern Pacific. The



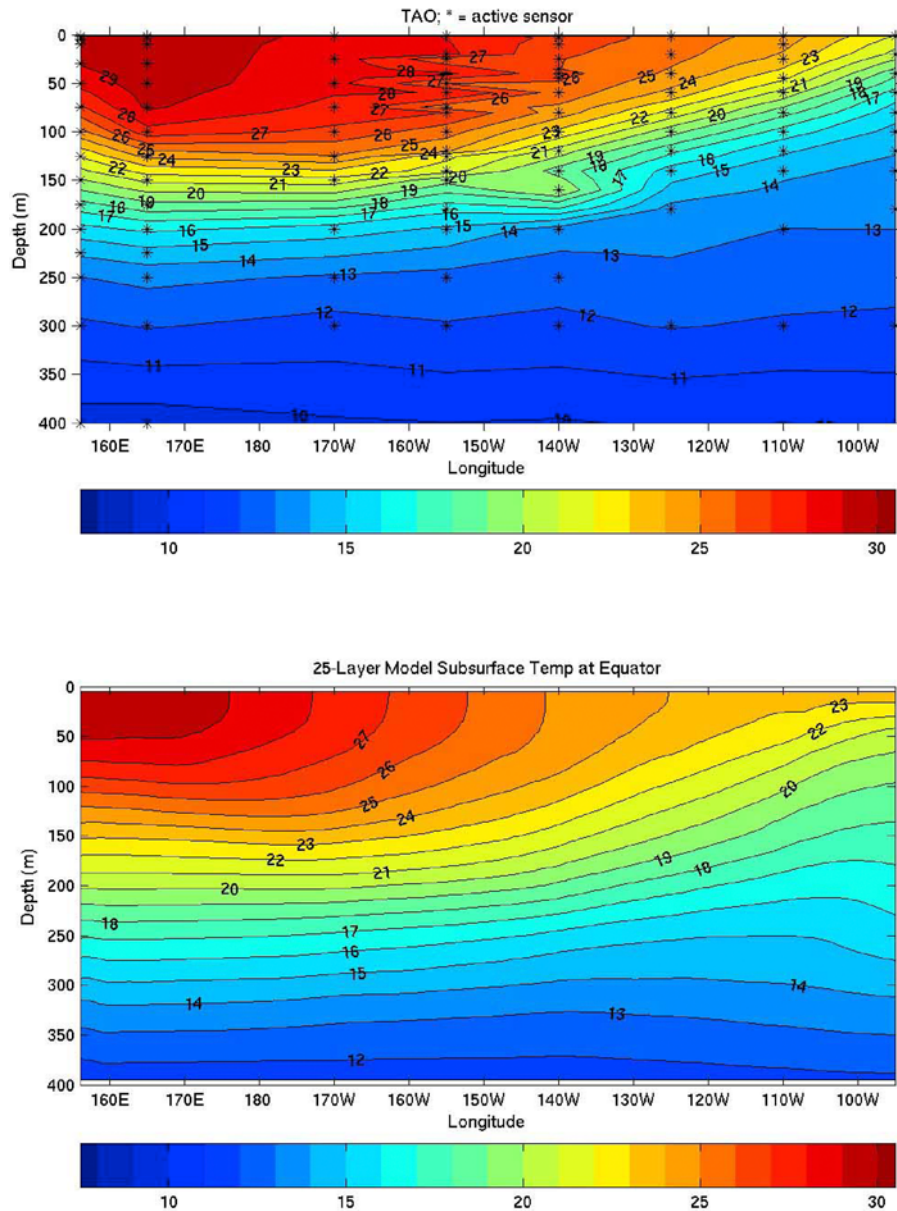


**Figure 6.** Annual mean subsurface temperature (0–400 m) for the equatorial Pacific Ocean from January 1990 to December 1992. (top) Subsurface temperature from TAO buoys located on the equator; asterisks mark the locations of active temperature sensors. (bottom) Subsurface temperature from the 25 layer model at the equator.

modeled SST response reproduces many of the large-scale SST variations that are observed by TAO SST (Figure 5 (middle)). The model shows good agreement with the timing of variations in SST but is slightly biased cold compared to the observed anomalous SST. The maximum bias in the modeled Nino3 region anomalous SST is about  $1^{\circ}\text{C}$  during the 1997–1998 El Niño.

[33] A comparison of the subsurface temperature structure of the equatorial Pacific basin for both the TAO buoy data set (Figure 6 (top)) and the modeled ocean (Figure 6 (bottom)) is shown in Figure 6. Figure 6 is constructed using pentad-averaged TAO and model data from 1 January 1990 to 31 December 1992 sampled at the equator. Since the TAO subsurface sensors are on a nonuniform grid (i.e., each buoy

may or may not measure the same depth level as its neighbor, see  $125^{\circ}\text{W}$  buoy compared to the  $110^{\circ}\text{W}$  buoy in the upper 100 m; sensor placement is marked by an asterisk), the data was placed on a uniform grid that accounts for all available sensor depths; depths without sensors were marked as missing data. An annual cycle was produced from the three years of data then that annual cycle was temporally averaged to produce the mean average subsurface temperature shown in Figure 6. The data shown in Figure 6 are vertically interpolated through unused levels. The TAO data was not temporally interpolated. The western warm pool (defined here as SST greater than  $29^{\circ}\text{C}$ ) in the model is smaller at the surface and more shallow than that of the TAO data. In the eastern Pacific (east of  $120^{\circ}\text{W}$ ), surface water temperatures in the

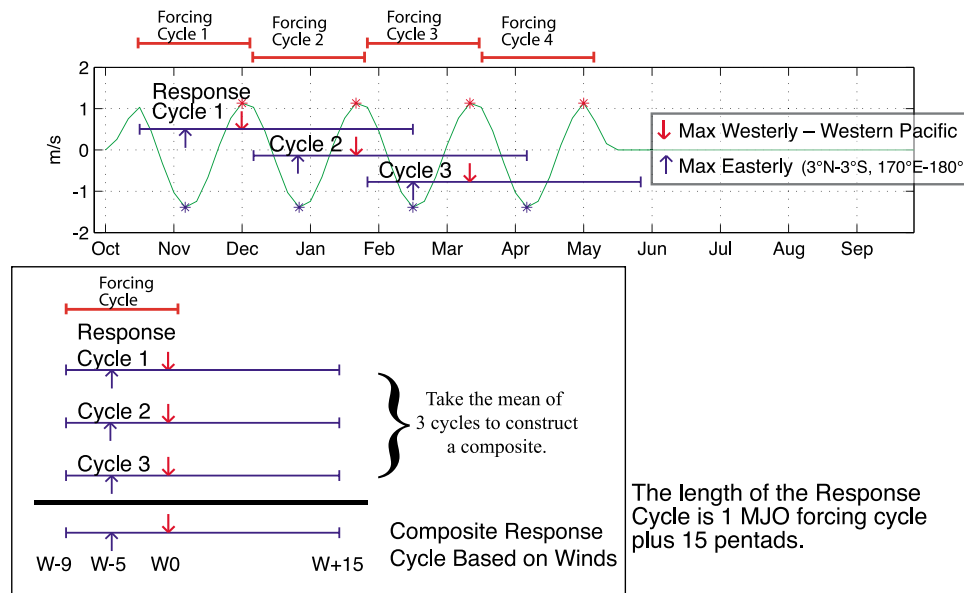


**Figure 7.** Graphical representation of the compositing technique and the time descriptor, W0. Spatially averaged MJO wind forcing from 3°N to 3°S and 170°E to 180°E (green line). Red asterisks and arrows denote maximum westerly wind forcing. Blue asterisks and arrows denote maximum easterly wind forcing.

model are on the order of 23°C and are within a  $\pm 1^\circ\text{C}$  range of the TAO data. The mean annual vertical temperature gradient produced by the model is weaker in the mixed layer region (i.e., the upper 100 m) ( $\sim 4.5^\circ\text{C}/100\text{ m}$ ,  $\sim 3^\circ\text{C}/100\text{ m}$ ) compared to the observed ( $\sim 7^\circ\text{C}/100\text{ m}$ ,  $\sim 7^\circ\text{C}/100\text{ m}$ ) at 95°W and at 120°W, respectively. Recent results from *Karnauskas et al.* [2007] show that the Gent and Cane OGCM's eastern Pacific cold tongue bias could be improved by the inclusion of the Galápagos Islands coastline. The presence of these island features in the eastern Pacific acts as an obstruction of the Equatorial Undercurrent (EUC) and, through an equatorial dynamical adjustment, can produce a deeper thermocline, warmer SST and an improved subsurface temperature structure.

[34] In general, the OGCM performed well at reproducing a realistic mean annual SST structure of the equatorial Pacific and was capable of simulating realistic SST variability. However, there is a SST bias on the order of 1°C in the eastern Pacific as well as weaker vertical temperature gradients compared to observations which, especially the latter, is relevant to the study's findings and caveats discussed in section 4.

### 3.2. Eastern Pacific Ocean Model Response to MJO Forcing

[35] Simulations forced by climatological forcing plus MJO anomalies were performed to quantify the ocean response to MJO forcing. The anomalous response was determined by calculating the differences between the MJO-forced response and the response to climatological forcing. The simulation timeframe is one year beginning on October 1. The forcing contains 4 cyclic events of idealized wintertime MJO forcing with each event lasting 10 pentads (see Figure 4 and section 2.3).

[36] A composite ocean response, relative to a given time in the MJO forcing cycle, was computed by averaging the

anomalous ocean response over each of three MJO events plus a lagged response window. The response from the fourth cycle was not included in the composite due to the length of the forcing record and length of the lag window. The method of compositing and the definition for a time descriptor (i.e., the given time in the MJO forcing cycle based on MJO zonal winds) are shown graphically in Figure 7. The composite window is 25 pentads and is composed of one MJO forcing event (10 pentads) plus an additional 15 pentads to accommodate the lagged response window. The length of the lagged response window was chosen to be long enough to capture the observed lagged correlation between intraseasonal zonal winds in the western Pacific (on the equator at 180) and intraseasonal SST (on the equator at 110°W) taken from the TAO buoys at those locations (+11 pentads between observed intraseasonal winds and observed SST response which accounts for the ocean Kelvin wave propagation from the

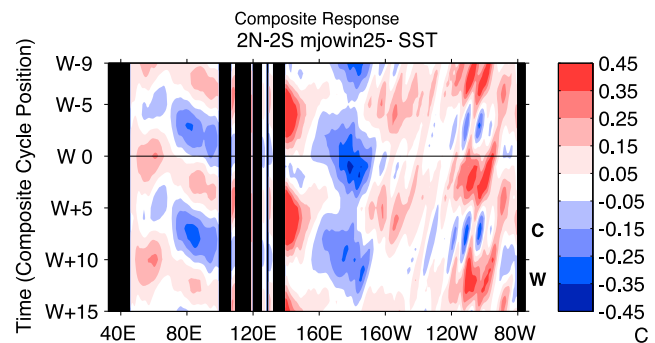


**Figure 8.** Time-longitude plot of the anomalous SST ocean response averaged 2°N–2°S. Black line is placed to mark the time W0, the time of maximum westerly wind forcing in the region of 3°N–3°S, 170°E–180°E. “W” and “C” on the right-hand axis mark the warming and cooling event, respectively, presented and discussed section 3.2.1.

## Composite Response

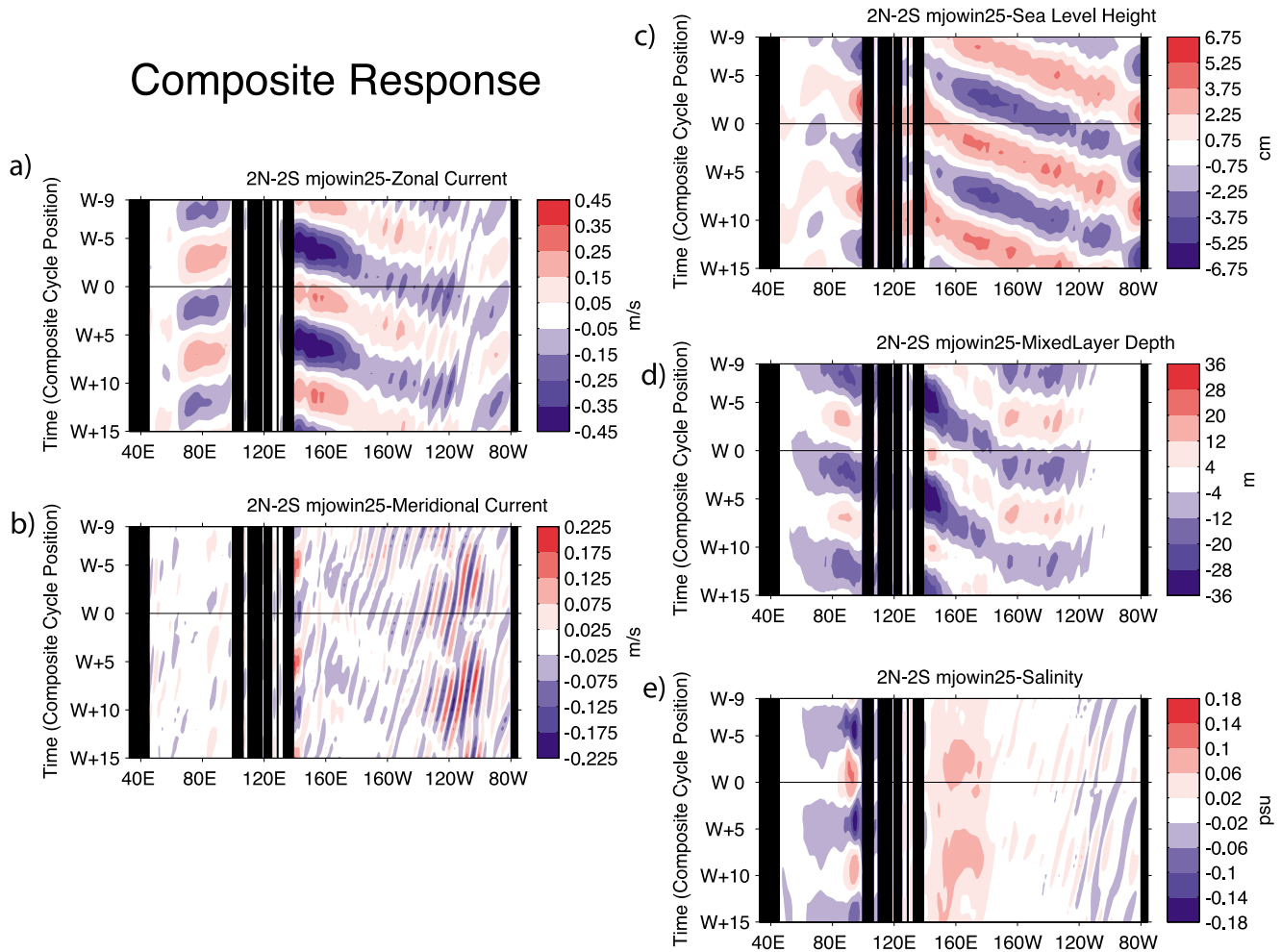


**Figure 9.** Spatially averaged 2°N–2°S time longitude diagram of (a) zonal and (b) meridional current, (c) mixed layer depth, (d) sea level height, and (e) salinity. Black line is placed to mark the time W0, the time of maximum westerly wind forcing in the region of 3°N–3°S, 170°E–180°E.

western to eastern Pacific, +10 pentads for the modeled ocean sampled at locations similar to those of the buoys; not shown).

[37] In Figure 7, the notation of W0 corresponds to the time at which there is maximum westerly wind forcing in the western Pacific (red asterisks and arrows). Maximum westerly wind forcing was determined by spatially averaging the zonal wind in the region from 3°N–3°S and 170°E–180°E (green line). Maximum easterly wind forcing occurs one-half MJO cycle earlier (i.e., –5 pentads) at W – 5 (blue asterisks and arrows). The period from W – 9 to W0 is 10 pentads of MJO forcing, or a complete forcing cycle. Thus, for the purpose of the discussion of Figure 7 and Figures 8–12, which follow in this section, a westerly (or easterly) MJO wind event occurs at W0 (or W – 5). The temporal response of the ocean is calculated relative to W0 with W + 1 being one pentad after the wind event, W + 2 two pentads after, and so on.

[38] It should be noted that due to the way the compositing is constructed, the designated forcing period (i.e., W – 9 to W0) for cycles 2 and 3 overlap with the previous MJO forcing cycle’s ocean response. For example, in Figure 7 the second western Pacific wind-forcing cycle overlaps the first

eastern Pacific response cycle. Therefore, when composited, the response shown during the period of W – 9 to W0 is the average response to both the local forcing and the response remotely forced (i.e., via Kelvin waves) from the prior MJO forcing cycles (i.e., cycles 1 and 2). For the purpose of clarity in the temporal and spatial description below, the SST response that will be discussed in detail will be the one that occurs at least 10 pentads (i.e., period of lag between maximum wind and SST correlation) after maximum westerly winds (W0) or maximum easterly winds (W – 5). The SST response will be split into two phases, a warm phase and a cold phase, and discussed individually. Additionally, the transition from the cold phase to the warm phase (i.e., the time prior to maximum positive SST anomaly) will be referred to as “warming” or “warming phase” whereas the transition from warm phase to cold phase (i.e., the time prior to the minimum SST anomaly) will be referred to as “cooling” or “cooling phase.”

### 3.2.1. Description of Temporal and Spatial Variability of Ocean Model Response: Warm and Cold Phases

[39] Figure 8 shows the time-longitude evolution of composite anomalous ocean response in terms of SST averaged at the equator from 2°N to 2°S. The time evolution of

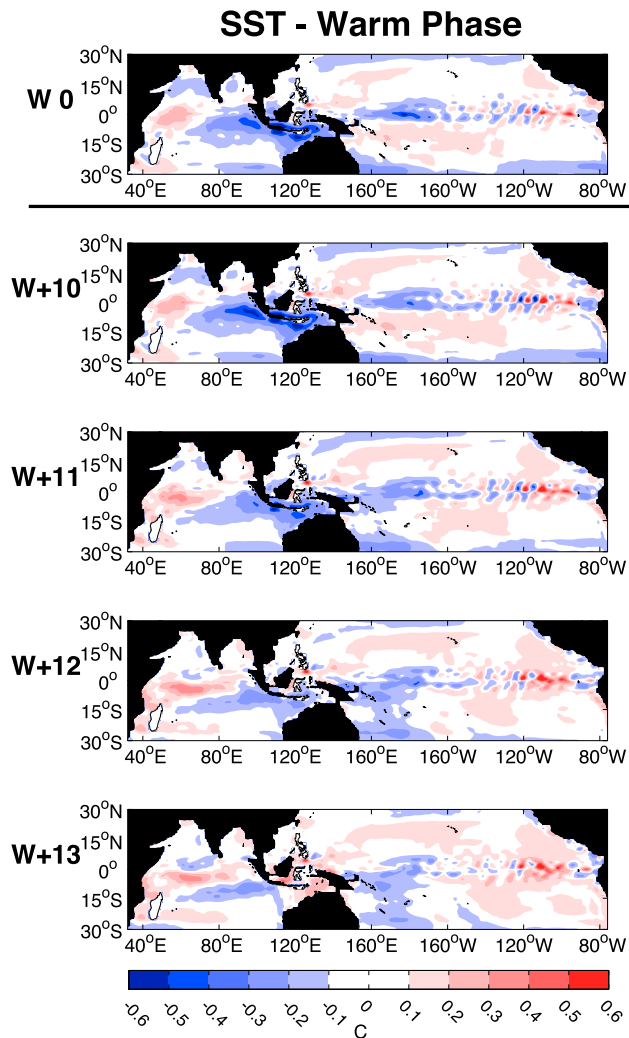


**Figure 10.** Warm phase composite ocean model SST response to three cycles of MJO forcing. W + 10 to W + 13 are relative to the maximum westerly wind in the western Pacific (W0). W + 10 is 10 pentads (50 days) later, W + 11 is 11 pentads later, and so on.

the SST in the eastern Pacific shows a large ( $\sim 25^\circ$  longitude) periodic pattern of warming and cooling on the order of  $0.4^\circ$  C. The period of the combined warming and cooling cycle is approximately 10 pentads. As noted above, the composite response shows two warmings and one cooling in the eastern Pacific that were initiated prior to W0, seen at W - 9, W - 1 and W - 5, respectively. These result mainly from the inclusion of (in the composite) the ocean response from the prior MJO event. To ensure that the warming (or cooling) event in the eastern Pacific examined here is the one that is remotely forced (i.e., one that develops at least 10 pentads after maximum westerly winds), only the events marked on the right-hand axis in Figure 8 as “W” (or “C”), will be discussed here after.

[40] Figure 9 shows the time-longitude evolution for the anomalous composite surface response in terms of zonal and meridional current, mixed layer depth, sea level height and salinity averaged from  $2^\circ\text{N}$  to  $2^\circ\text{S}$ . Zonal current (Figure 9a), sea level height (Figure 9c) and mixed layer depth (Figure 9d)

all show the initiation of a downwelling Kelvin wave (at W0) generated by the increasing westerly MJO winds in the western Pacific. The Kelvin wave is the eastward propagating region of eastward current (red) and increased sea level height (red) which starts in the western Pacific and travels toward the eastern Pacific arriving at  $100^\circ\text{W}$  at approximately W + 6. Zonal current and sea level height displacement for the warm (cold) phase are on the order of 30 cm/s ( $-30$  cm/s) and 4 cm ( $-4$  cm), respectively. The mixed layer response in the western and central Pacific shows a deepening mixed layer (red) on the order of 4 to 20 m ( $-4$  to  $-20$  m, cold phase) however, in the far eastern Pacific the mixed layer is only minimally affected (less than 4 m for both phases) by MJO forcing. Meridional currents (Figure 9e) in the eastern Pacific are on the order of 10 cm/s and are influenced by the presence of westward propagating tropical instability waves (TIWs).

[41] The spatial extent of the warm phase evolution in terms of SST, zonal current, and meridional current is shown in Figures 10–12. The phase evolution shown in Figures 10–

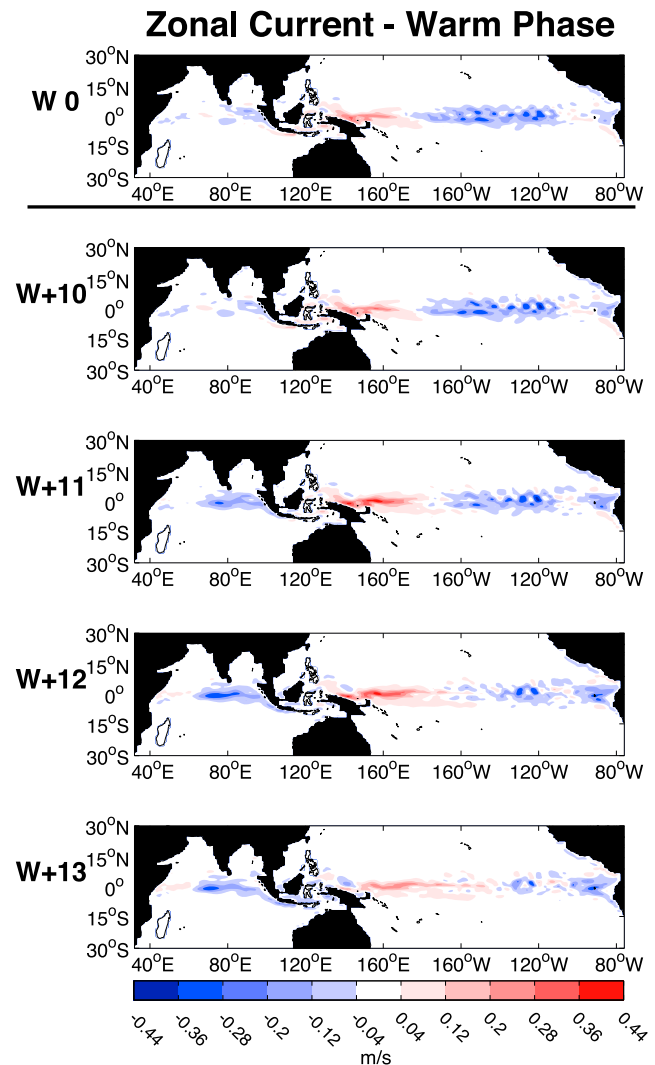


**Figure 11.** Same as Figure 10 except zonal current response to three cycles of MJO forcing. W + 10 to W + 13 are relative the maximum westerly wind in the western Pacific (W0).



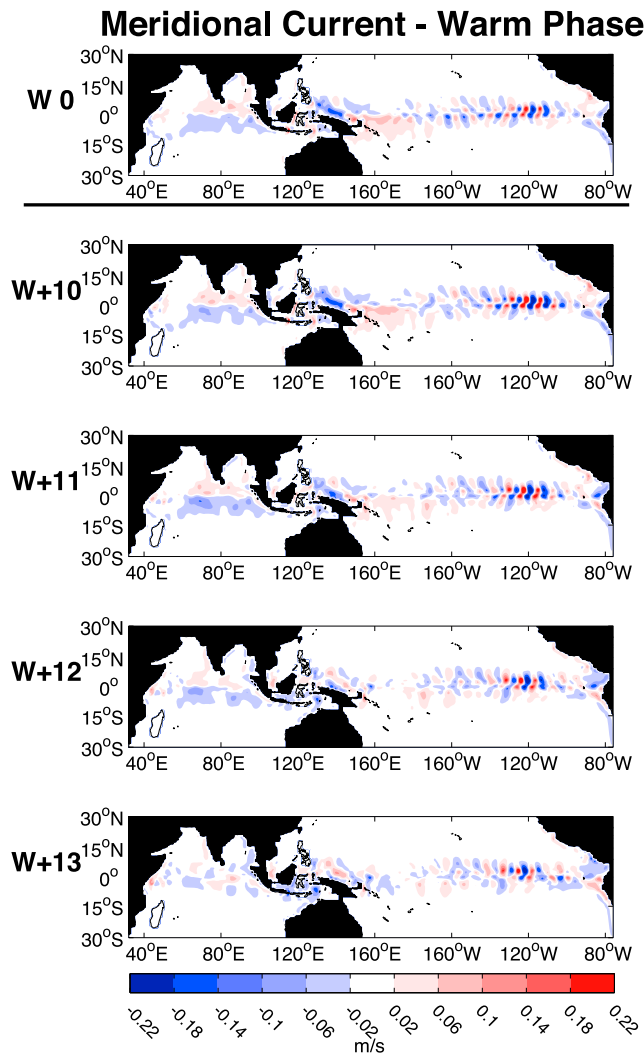


**Figure 12.** Same as Figure 10 except meridional current response to three cycles of MJO forcing. W + 10 to W + 13 shown are relative the maximum westerly wind in the western Pacific (W0).

12 is W0 (the time of peak westerly wind forcing), W + 10 (10 pentads later during the peak rate of SST warming), and 1 pentad intervals up to W + 13 (the peak SST anomaly). On a basin-wide scale these results for the most part show the expected response in the Indian and Pacific Oceans and are consistent with the previous studies discussed in the introduction. Since the focus of this work is the tropical Pacific, hereafter the discussion will be limited to that region. Due to the similarity in the structure of the response between the warm and cold phases, only the warm phase will be presented. The cold phase response will be described in relation to the warm phase.

[42] The most obvious feature of the anomalous SST warm phase response in the eastern Pacific (Figure 10) is the systematic warming in W + 11 through W + 13. The maximum SST change in the eastern Pacific is on the order of  $0.5^{\circ}\text{C}$  and is confined to the equatorial region. The perturbation in W + 13 (the peak anomalous SST) extends approximately  $25^{\circ}$  in longitude (2750 km) from  $95^{\circ}\text{W}$  to  $120^{\circ}\text{W}$  and from  $3^{\circ}\text{N}$  to  $3^{\circ}\text{S}$  in latitude (660 km). The

longitudinal center of the peak SST perturbation is zonally stationary in time at approximately  $110^{\circ}\text{W}$  (also seen in Figure 8), however the western edge grows slightly to the west over time by approximately  $10^{\circ}$  longitude.

[43] For the cold phase, the peak easterly wind event occurs at W – 5. The corresponding development of the cold phase is weaker and less spatially coherent than the warm phase. The minimum anomalous SST in the cold phase is on the order of  $-0.3^{\circ}\text{C}$  when averaged over  $2^{\circ}\text{N}$  to  $2^{\circ}\text{S}$ . The zonal structure is approximately  $100^{\circ}\text{W}$  to  $120^{\circ}\text{W}$  (2200 km) however, there is a region of persistent weak SST anomaly ( $\sim 0.1^{\circ}\text{C}$ ) to the west at  $140^{\circ}\text{W}$ . These results are consistent with the SST perturbations that are found in observations and those that have been described by Zhang [2001], McPhaden [2002], and others listed in the introduction.

[44] For the warm phase, the surface currents in Figures 11 and 12 show that the spatial extent of the zonal and meridional current is confined to the equatorial region. Meridional currents show the signature undulating pattern of TIW activity in the eastern Pacific. The zonal current in Figure 11 shows that during the last 3 pentads of the warming phase of SST, there is the presence of an upwelling Kelvin wave arriving in the eastern Pacific (i.e., westward current (blue) propagating eastward at the equator). For the cold phase, the zonal current (not shown) exhibits the presence of a downwelling Kelvin wave (eastward current) arriving in the eastern Pacific around the time of W + 6.

[45] Keep in mind that the Zhang hypothesis suggests that SST warming is due to the presence of a downwelling Kelvin wave in the eastern Pacific (via the suppression of cooling from vertical advection). However, in Figure 9, the modeled downwelling Kelvin wave that was initiated at time W0 arrives in the eastern Pacific during the cold phase at W + 6, a time just before the warm phase of SST develops. This suggests that the downwelling Kelvin wave may act to initiate the transition from the cold phase to warming phase but, based on the presence of an upwelling Kelvin wave in the eastern Pacific several pentads prior to the maximum SST, the SST warming may not be maintained solely by Kelvin wave activity.

[46] From Figures 7–12 alone it is impossible to distinguish whether the heating cycle in the eastern Pacific is derived from local surface heat flux, remotely forced via Kelvin waves as shown by Zhang [2001], or through other ocean dynamics. A mixed layer heat budget will be pre-

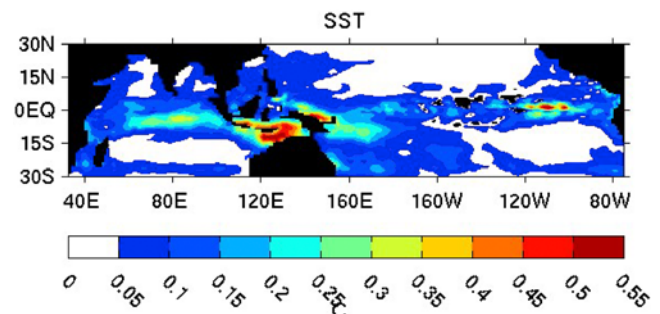


**Figure 13.** Variability associated with MJO forcing during the months of October–May. Variability is shown in terms of standard deviation. Please see text for a detailed description of the construction of this variability.

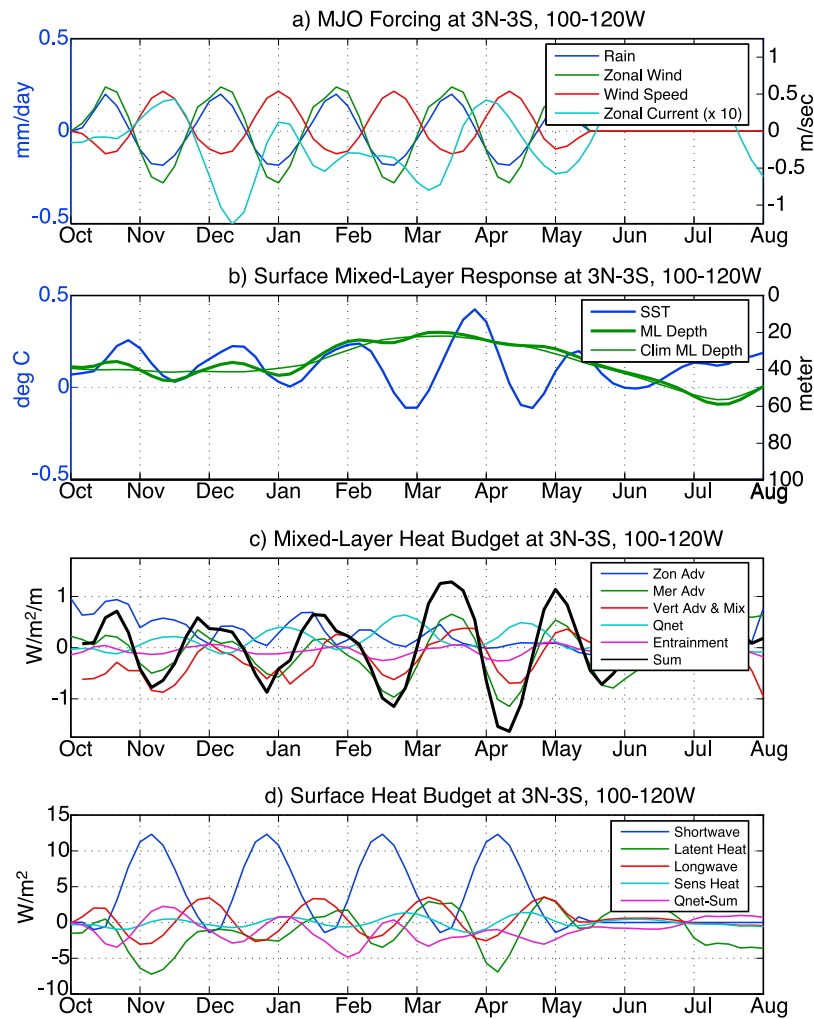


**Figure 14.** Local forcing, mixed layer response, and surface layer heat budget for eastern Pacific. Time series averaged over the region of  $3^{\circ}\text{N}$ – $3^{\circ}\text{S}$  and  $120^{\circ}\text{W}$ – $100^{\circ}\text{W}$  showing (a) local zonal wind, wind speed and rain forcing, and zonal current; (b) SST and mixed layer depth response; (c) ML heat budget; and (d) surface layer heat budget.

sented in section 3.2.2 to ascertain the sources of heating and cooling in the eastern Pacific.

### 3.2.2. Mixed Layer Heat Balance

[47] To establish a more detailed analysis of the surface ocean response in the eastern Pacific, a regionally averaged surface layer heat budget was constructed. The selection of the region is based on the area of maximum SST variability forced by MJO (Figure 13). The variability shown in Figure 13 is constructed relative to the internal variability that is shown in Figure 2. In general, the method used to calculate variability of a system is fairly straightforward. However, variability in the OGCM's SST response contains both variability associated with MJO forcing and internal variability of the model (i.e., variability in the climatology-forced response that is not associated with the mean annual cycle response; for example, TIWs). In order to construct the variability shown in Figure 13, careful attention must be paid to separate the MJO-forced variability from the internal variability. First, the anomalous ocean response, relative to

the annual cycle, was computed at each grid point. Then the variance of the anomalous response was computed at each grid point. Since MJO forcing is applied only during the months of October to mid-May, those pentads were used to compute a spatial map of mean variance similar to that shown in Figure 2. That mean variance map (not shown) contains MJO-forced variability plus internal variability [cf. *Waliser et al.*, 2003]. To estimate the portion of variance associated with the MJO forcing, the model's internal variability during the period of October to mid-May (discussed in section 2.2; Figure 2) was subtracted. Figure 13 is shown in terms of standard deviation. The region of highest variability in the eastern Pacific is from  $3^{\circ}\text{N}$  to  $3^{\circ}\text{S}$  and  $120^{\circ}\text{W}$  to  $100^{\circ}\text{W}$ . This region will be used for further examination of the intraseasonal SST relationship. In this region the maximum standard deviation for SST is  $0.54^{\circ}\text{C}$ .

[48] Figure 14 presents the surface layer heat budget, local wind and rain (freshwater) forcing, and the mixed layer response averaged over the region of maximum SST vari-

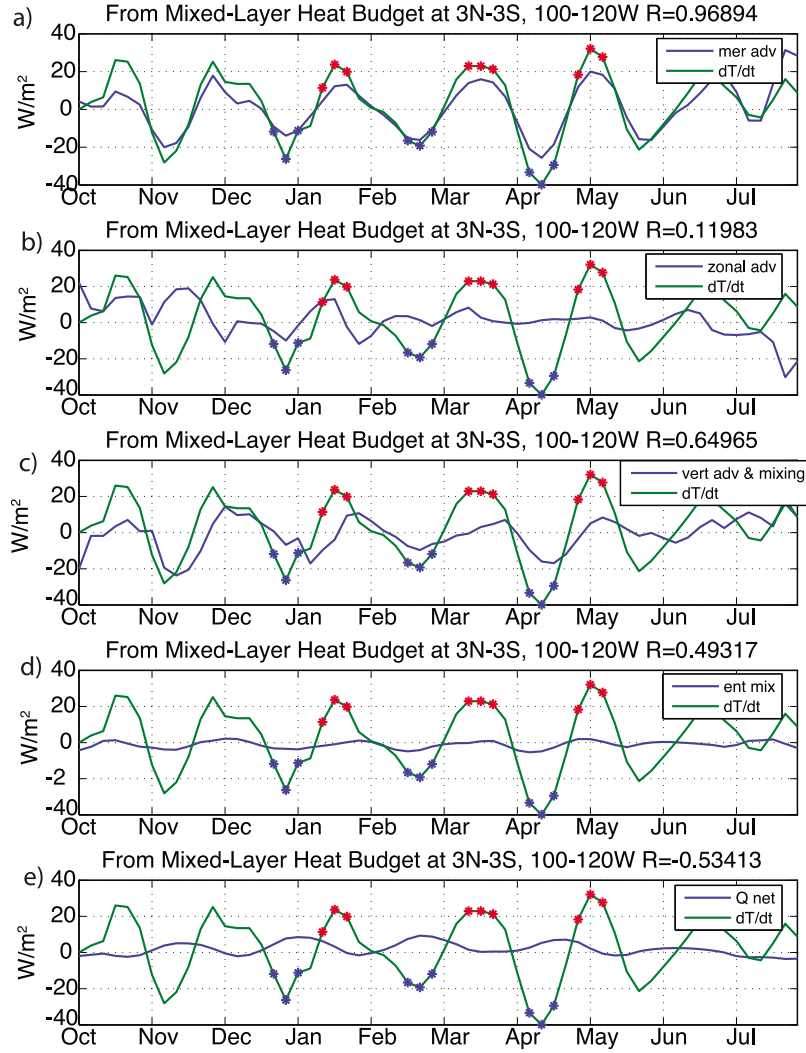


**Figure 15.** Comparison of the relative contribution to  $dT/dt$  for the mixed layer heat budget terms listed in Figure 14c and the time rate of change for anomalous SST ( $dT/dt$ ) (green line; shown as  $W/m^2$ ) for (a) meridional advection (blue line), (b) zonal advection (blue line), (c) vertical advection and mixing (blue line), (d) entrainment (blue line), and (e)  $Q_{net}$  (blue line). Red (blue) asterisks are those warming (cooling) events included in composite warming (cooling) calculations.

ability ( $3^{\circ}N-3^{\circ}S$ ,  $120^{\circ}W-100^{\circ}W$ ). The surface layer heat budget is based on the following equations:

$$\frac{\partial T}{\partial t} = \frac{Q_{net}}{H\rho_0 C_p} - u \frac{\partial T}{\partial x} - v \frac{\partial T}{\partial y} - w \frac{\partial T}{\partial z} + \text{entrainment} + \text{mixing}, \quad (1)$$

$$Q_{net} = (1 - \alpha)SW - [LW + LH + SH] - SW_B, \quad (2)$$

where  $Q_{net}$  is the net surface heat flux from the atmosphere above,  $SW$  is the incoming solar shortwave radiation which is reduced by the surface albedo ( $\alpha$ ),  $LW$  is the net longwave radiation,  $LH$  is the latent heat flux,  $SH$  is the sensible heat flux, and  $SW_B$  represents the portion of  $SW$  radiation lost by penetration below the mixed layer;  $\rho_0$  is seawater density,  $C_p$  is heat capacity,  $H$  is mixed layer depth, and  $T$  is mixed layer temperature. In the first equation,  $dT/dt$  represents the time rate of mixed layer temperature change balanced by the

net surface heat flux, horizontal and vertical advection terms ( $-u \frac{dT}{dx}$ ,  $-v \frac{dT}{dy}$ ,  $-w \frac{dT}{dz}$ ), entrainment, and horizontal and vertical mixing terms. Horizontal advection, entrainment and  $Q_{net}$  were calculated by the model in terms of  $W/m^2$  and are shown in Figure 14c as spatially averaged pentad mean values per meter of mixed layer depth (i.e.,  $W/m^2/m$ ). To calculate the spatially averaged values, mixed layer depth at individual grid points were used prior to spatially averaging. Here  $\frac{dT}{dt}$  is calculated using the time rate of change of the spatially averaged pentad mean SST anomaly (i.e.,  $\frac{dT}{dt} = SST_{t+1} - SST_t$ ). The vertical advection and mixing terms, both horizontal and vertical, are collected into one term and were calculated as a residual difference using

$$\left[ -w \frac{dT}{dz} + \text{mixing} \right] = \frac{dT}{dt} - \left[ \frac{Q_{net}}{H\rho_0 C_p} - u \frac{dT}{dx} - v \frac{dT}{dy} + \text{entrainment} \right]. \quad (3)$$

**Table 1.** Summary of the Mixed Layer Heat Budget Terms Contributing to the Warming and Cooling Events in the Composite Anomalous SST Response Shown in Figure 15

	Warming Phase		Cooling Phase	
	W/m <sup>2</sup>	Percent of total budget	W/m <sup>2</sup>	Percent of total budget
Zonal advection	4.55	20.5	-1.11	5.0
Meridional advection <sup>a</sup>	13.75	61.8	-15.71	70.7
Vertical advection and mixing terms	1.49	6.7	-8.33	37.6
Entrainment	0.34	1.5	-3.86	17.4
Net surface heat flux	2.11	9.5	6.82	-30.7
Rate of mixed layer temperature change ( $dT/dt$ )	22.24 (0.10°C/pentad)	100	-22.20 (-0.11°C/pentad)	100

<sup>a</sup>This is the largest contributor.

[49] The vertical advection and mixing term is calculated for this heat budget as a residual due to difficulties that arise from transforming vertical velocity ( $w$ ) from a sigma based coordinate system to depth based  $z$  coordinates. It should be noted that a sigma layer model does not use a vertical advection term in the manner that a level model would. In a sigma layer model, the surface mixed layer is a variable depth layer. The calculation of mixed layer depth is done as a balance between surface turbulent kinetic energy (TKE) and stratification rather than as a series of levels with an interface through which vertical advection would pass (i.e., a fixed depth levels). Therefore, entrainment is the most important vertical term when using a moving interface (i.e., the bottom of the mixed layer) and vertical advection and mixing should be calculated as the residual of the heat budget.

[50] The anomalous SST response (Figure 14b) shows a fair amount of variability in the first 3–4 months even though this is primarily associated with weak local MJO forcing (i.e., zonal wind less than 0.5 m/s, rain less than 0.1 mm/d, Figure 14a) in this region. Also evident is the long delay in the zonal current response (Figure 14a), nearly one and a half months after MJO forcing begins. The lack of strong local forcing, the long lag in the zonal current response, taken together with the composite zonal current and sea level height discussed above suggests that at least a portion of the anomalous SST is forced remotely by winds to the west and possibly influenced by Kelvin or other wave activity.

[51] SST variations are on the order of 0.5°C and have very little mixed layer depth variability associated with them (when averaged over the region). Figure 14c shows that the primary contributors to the SST anomalies are meridional advection, and the vertical advection and mixing term. Each are large in magnitude at times leading SST change.

[52] However, a better way to compare the contributing terms in the mixed layer heat budget is to examine each term individually for the relative contribution to  $dT/dt$  and the degree to which the term and  $dT/dt$  are correlated. Figure 15 shows the relative contribution to  $dT/dt$  (green line; shown as W/m<sup>2</sup>) for meridional advection (Figure 15a, blue line), zonal advection (Figure 15b, blue line), vertical advection and mixing (Figure 15c, blue line), entrainment (Figure 15d, blue line), and  $Q_{net}$  (Figure 15e, blue line); asterisks denote times the maximum warming (red) or cooling (blue) rates for the composite period. Meridional advection is larger and better correlated with the time rate of change of SST ( $r = 0.97$ ) than vertical advection and mixing ( $r = 0.65$ ). Zonal advection is roughly equal in magnitude to vertical advec-

tion and mixing but its phase leads SST change by a small degree.  $Q_{net}$ , the amount of surface heat flux that is retained in the mixed layer, is mostly positive, small (~5–10 W/m<sup>2</sup>) and anticorrelated with  $dT/dt$  ( $r = -0.53$ ) suggesting that it contributes both to reducing the total amount of cooling during the cold phase and helps to initiate the warming phase. Entrainment contributes to cooling the mixed layer during the cold phase, leading the time of surface SST cooling by about a quarter cycle. The peak warming rate of  $d(SST)/dt$  is approximately 0.14°C/pentad in late April/early May (shown as W/m<sup>2</sup>). The peak cooling rate is approximately -0.17°C/pentad in early April (shown as W/m<sup>2</sup>).

[53] Composite averages are used to determine the contributors to the mean warming and cooling of SST from the cyclic MJO forcing events described above. The events are chosen based on maximum warming (or cooling) rates and include the time one pentad prior to and one pentad after the maximum rate. The selected events are highlighted by the 9 red (9 blue) asterisks on Figure 15. Table 1 shows the composite SST response from the 3 events (total of 9 pentads averaged) and the mixed layer heat budget for both the cold and warm phase in terms of W/m<sup>2</sup> and percentage of the total budget. The composite response shows that meridional advection accounts for the bulk of the SST change (61.8% warming; 70.7% cooling) followed by vertical advection and mixing (6.7% warming; 37.6% cooling). Zonal advection (20% warming; 5% cooling) and net surface heat flux (9.5% warming; -30.7% cooling) play important roles in the development of warm SST events whereas entrainment (1.5% warming; 17.4% cooling) is important in the formation of the cold events.

[54] To determine the relative importance of the mean advection and eddy terms to the total meridional advection, the mean and eddy components were calculated and are presented in Figure 16. This partitioning tests the relative importance of: 1) advection of the MJO-forced (i.e., anomalous) temperature field by mean currents ( $-\bar{v} \frac{dT'}{dy}$ ), 2) MJO-forced advection of the mean temperature field, ( $-\bar{v}' \frac{dT}{dy}$ ), and 3) the interaction of MJO-forced currents and the MJO-forced temperature field ( $-\bar{v}' \frac{dT'}{dy}$ ), where bars (e.g.,  $-\bar{v}$ ) represent the climatological mean and primes (e.g.,  $-\bar{v}'$ ) represent the anomaly. Results for the 9 warming pentads (9 cooling) used for the composite mixed layer heat budget discussed above are shown in Table 2. The “Composite Response” column lists the phase of the composite response; the “ $-\bar{v} \frac{dT'}{dy}$ ,” “ $-\bar{v}' \frac{dT'}{dy}$ ,” and “ $-\bar{v}' \frac{dT}{dy}$ ” columns list the values for the calculated eddy terms; and the “ $-\bar{v} \frac{dT}{dy}$ ” column lists the values for the mean climatological meridional advection. The



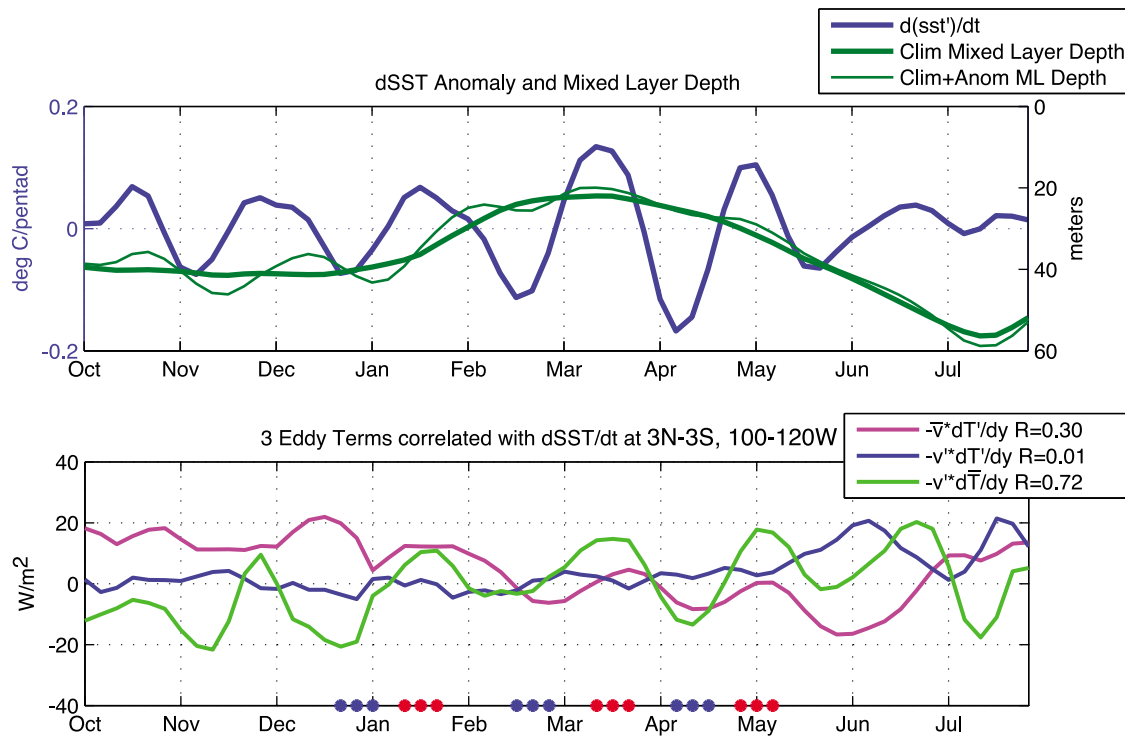


**Figure 16.** Calculated meridional advection eddy terms. (top) Rate of mixed layer temperature change (blue line, left-hand axis), mixed layer depth in terms of climatological value (thick green line, right-hand axis), and the sum of the climatological and anomalous value (thin green line, right-hand axis). (bottom) Calculated meridional advection eddy terms (see inset legend). Red (blue) asterisks are the warming (cooling) events included in composite warming (cooling) calculations.

uncertainty listed in the “Uncertainty in Calculated Terms” column refers to the “degree of approximation” introduced by the use of a 5 day mean value of meridional current ( $v$ ) and temperature ( $T$ ) used to calculate the eddy terms. This uncertainty is calculated from the difference between the sum of the calculated eddy terms at any given time (shown in Table 2) and the anomalous meridional advection recorded by the model at that time. This uncertainty primarily results from the loss of variance due to multiplying two averaged terms (i.e.,  $-v dT/dt$ ) rather than multiplying two fluctuating terms prior to averaging. There is no approximation uncertainty in the mean meridional advection term as its value (shown in Table 2) is calculated by the model. MJO-forced advection of the mean temperature field ( $-v' \frac{d\bar{T}}{dy}$ ) is the leading term driving the meridional advection in both the

warming and cooling phase. Additionally,  $-v' \frac{d\bar{T}}{dy}$  is better correlated with  $dT/dt$  ( $r = 0.72$ ) and contains more variance ( $118.3 (W/m^2)^2$ ) than the second leading term  $-\bar{v} \frac{dT'}{dy}$  ( $r = 0.2$ ,  $83.2 (W/m^2)^2$ ) during the time of MJO forcing. In section 4, these results are summarized and put in to context with previous studies mentioned in the introduction.

#### 4. Summary and Discussion

[55] The objective of this study was to explore the relationship between the atmospheric Madden-Julian Oscillation (MJO) and intraseasonal sea surface temperature (SST) variability in the eastern tropical Pacific Ocean. Investigating this relationship is important because changes in SSTs in the eastern Pacific Ocean could play a role in initiating and

**Table 2.** Mean and Eddy Components of the Anomalous Meridional Advection Associated With MJO Forcing<sup>a</sup>

Composite Response	$-\bar{v} \frac{dT'}{dy}$	$-v' \frac{dT'}{dy}$	$-v' \frac{d\bar{T}}{dy}$	Uncertainty in Calculated Terms	$-\bar{v} \frac{d\bar{T}}{dy}$
Warming events ( $W/m^2$ )	4.81	1.48	12.87	-3.56	-29.42
Cooling events ( $W/m^2$ )	0.36	0.15	-9.03	-3.84	-24.00
	$-\bar{v} \frac{dT'}{dy}$		$-v' \frac{dT'}{dy}$		$-v' \frac{d\bar{T}}{dy}$
Correlation with $dT/dt$	0.30		0.01		0.72
Variance ( $W/m^2$ ) <sup>2</sup>	83.17		10.97		118.3
Standard deviation ( $W/m^2$ )	9.12		3.31		10.88

<sup>a</sup>The uncertainty listed in the “Uncertainty in Calculated Terms” column refers to the “degree of approximation” introduced by the use of a 5 day mean value of meridional current ( $v$ ) and temperature ( $T$ ) used to calculate the eddy terms. This uncertainty is calculated from the difference between the sum of the calculated eddy terms at any given time and the anomalous meridional advection recorded by the model at that time. Correlation, variance, and standard deviation are taken for the first  $W + 1$  forcing period to the end of the forcing.

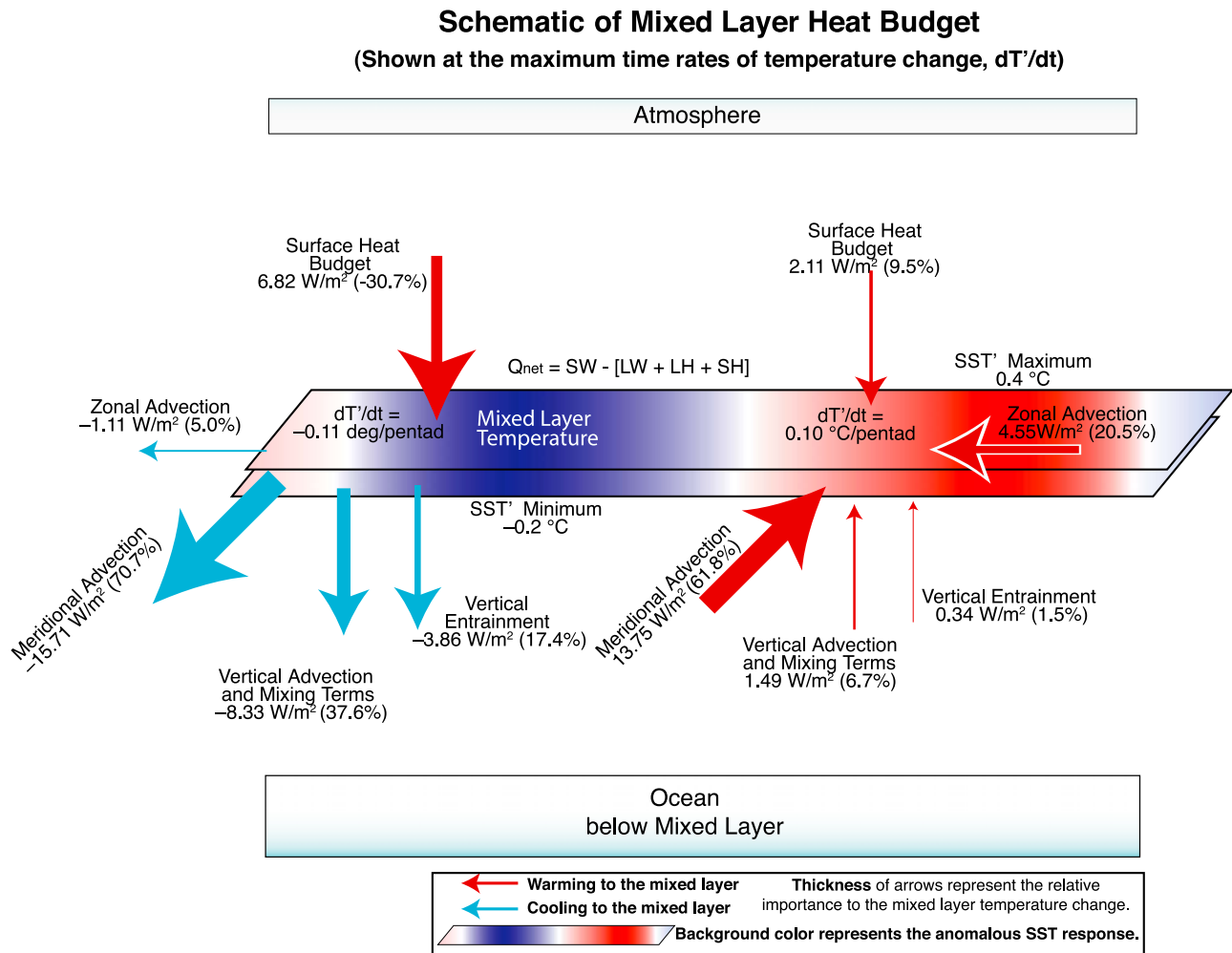


**Figure 17.** Schematic of mixed layer temperature balance for the warming (right, red) and cooling (left, blue) phase of intraseasonal SST. Thickness of the arrow shaft represents the relative importance of each term. Red background and arrows indicate warming, and blue background and arrows indicate cooling.

regulating El Niño/La Niña events. Previous observational studies by Zhang [2001] and McPhaden [2002] have illustrated the connection between the MJO and the development of zonally large ( $>2000 \text{ km}$ ) and persistent (on the order of weeks) SST anomalies. Those studies suggested that changes in vertical processes, such as vertical advection and entrainment, forced remotely by winds in the western Pacific (via equatorial Kelvin waves) may be the mechanism controlling SST changes. However, those studies were restricted by the use of a limited set of observations (e.g., sparse sampling and missing data) which did not allow for an exacting assessment of the mechanisms associated with intraseasonal SST variability in the eastern Pacific.

[56] An ocean general circulation model (OGCM) was employed in this study to compliment the above work and to possibly overcome the limitations of the observation-based studies with the goal of obtaining a more complete physical understanding of the ocean dynamic and thermodynamic processes associated with the development of the SST anomalies. The OGCM used in this experiment was tested using observed forcing fields of rain, wind, solar radiation, and cloud fraction. Validation of the modeled SST response

was based on climatological SST from Levitus and Boyer [1994] and the observed SST and subsurface temperatures used by Zhang [2001] and McPhaden [2002]. The OGCM was demonstrated to be capable of simulating realistic annual and interannual SST variability (Figure 5).

[57] The primary model simulation experiment used idealized MJO forcing constructed from observed fields. The results from this model experiment showed a SST response similar in spatial and temporal characteristics to the SST variability observed by Zhang [2001] (Figures 8 and 10). The model's wind/SST lag is similar to observations noted in literature with maximum SST anomalies developing 12 to 13 pentads (60–65 days) after the maximum zonal wind forcing in the western Pacific. Peak easterly (westerly) zonal wind forcing in the western Pacific initiated a Kelvin wave that propagates eastward and arrives in the eastern Pacific prior to periods of maximum SST cooling (warming). Contrary to Zhang's findings, the modeled downwelling Kelvin wave, which he hypothesizes to be the remotely forced link to SST warming, arrived at a time 2 to 3 pentads before the cold phase ends, well before the warming phase of SST develops. This modeled ocean response suggests that the downwelling

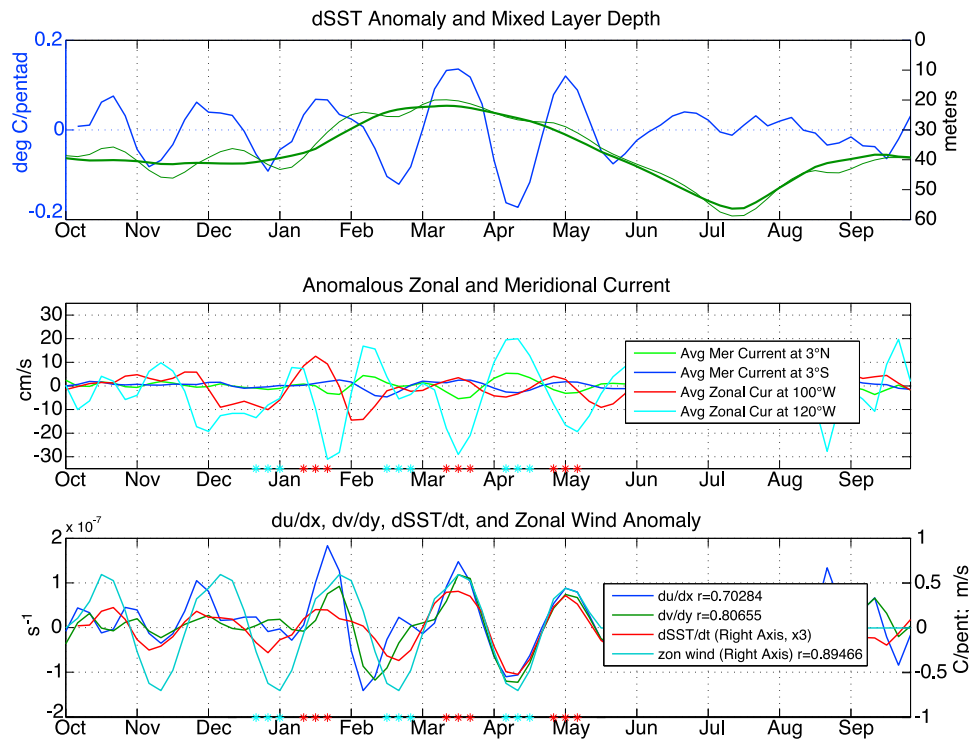


**Figure 18.** (top) Same as Figure 16 (top). (middle) Anomalous zonal and meridional currents. Zonal currents are meridionally averaged 3°N–3°S at the longitudes 100°W (red line) and 120°W (light blue line). Meridional current is zonally averaged 100°W–120°W at the latitudes 3°N (green line) and 3°S (dark blue line). Red (blue) asterisks denote the warming (cooling) events included in composite warming (cooling) calculations. (bottom) Zonal (dark blue line) and meridional (green line) convergence/divergence, time rate of SST change (red line, magnified three times), and zonal wind speed (light blue line). Correlation of dSST/dt is shown in the legend box.

Kelvin wave may act to initiate the transition from the cold phase to warming phase but that the SST warming may not be maintained solely by Kelvin wave activity.

[58] A mixed layer heat budget of the eastern Pacific during the cooling phase and the warming phase is summarized graphically in Figure 17. The thickness of the arrows represent the relative contribution to the mixed layer temperature change during periods of peak  $d(SST)/dt$ ; red arrows indicate warming, blue arrows indicate cooling. Analysis of the mixed layer heat budget shows that SST variability is primarily related to meridional advection, rather than vertical advection as suggested by the Zhang and McPhaden studies. Meridional advection accounts for 61.8% ( $13.75 \text{ W/m}^2$ ) of the warming phase and 70.7% ( $-15.71 \text{ W/m}^2$ ) of the cooling phase heat budget. Eddy term analysis shows that MJO-forced meridional currents are acting to redistribute the mean meridional temperature gradient. Zonal advection is the second largest term in the warming phase with 20.5% of the budget ( $4.55 \text{ W/m}^2$ ). Vertical processes (i.e., vertical advection and entrainment) play a significant role in the cooling phase (37.6%,  $-8.33 \text{ W/m}^2$  and 17.4%,  $-3.86 \text{ W/m}^2$ , respectively) however, surface heat flux acts to mediate the effect of cooling by warming the mixed layer ( $-30.7\%$ ;  $+6.82 \text{ W/m}^2$ ).

[59] Taking together all of the above discussion, the anomalous SST response is primarily driven by meridional advection (Table 1). Most of the meridional advection can

be attributed to the advection of the mean meridional temperature gradient by meridional currents forced by MJO (Table 2). During the warming phase, zonal advection plays a more significant role in the SST temperature change than vertical advection and mixing. However, during the cooling phase vertical advection and mixing, and entrainment are considerably larger terms than that of zonal advection.

[60] Although great care has been taken to ensure that the design of this experiment is robust, the limitations of this OGCM framework should be noted. First, this OGCM does use an atmospheric mixed layer model to calculate the surface heat flux but this OGCM is not a fully coupled ocean-atmosphere model. That is, SST does not have a feedback on the winds. Observed SST, like that analyzed by Zhang [2001] and McPhaden [2002], includes this feedback and other coupled phenomena of the ocean-atmosphere system. A future step may be to use a coupled ocean-atmosphere model to determine the implications on the findings presented here [cf. Zheng *et al.*, 2004]. Second, errors and limitations in the observed data used for the construction of forcing fields could lead to errors in the calculated response. In this study, careful attention was paid to obtain high-quality forcing data, to validate the OGCM to observed data, and to choose a model that has realistic fidelity at reproducing the tropical ocean response to MJO, as well as annual and interannual forcing. And lastly, the use of a mixed layer with a one-dimensional vertical mixing

scheme, and the assumptions that go with it (i.e., a well mixed, uniform temperature mixed layer), may not wholly represent all of the physical processes going on in our region of study.

[61] Additionally, it is important to understand the uncertainty associated with the OGCM's simulation of the meridional and vertical advection terms shown in the results of the surface layer heat budget. As discussed in section 2.2, the meridional SST gradient (Figure 1) and the vertical temperature gradient (Figure 6) contain biases in the annually averaged mean state. The magnitude of these biases can be used as a first-order estimate of the relative error between the meridional and vertical advection terms shown in the heat budget results (Table 1). The bias in the mean annual meridional SST gradient is small, on the order of a 10% over estimation, whereas the vertical temperature gradient in the model may be under estimated by almost a factor of 2. Using this as a guide, the results from the warming phase of the heat budget are relatively unchanged with meridional advection contributing  $12.38 \text{ W/m}^2$  and vertical advection and mixing terms contributing  $2.98 \text{ W/m}^2$ . However, the cooling phase heat budget may have almost equal contributions from meridional advection (accounting for  $14.14 \text{ W/m}^2$ ) and vertical advection and mixing terms ( $16.66 \text{ W/m}^2$ ). As discussed in section 3.1, the addition of the Galápagos Islands in future model experiments may act to reduce the bias in the eastern Pacific SST and the vertical temperature gradient which may have important implications on the results presented here.

[62] The primary result from this study, namely that MJO-forced meridional current is a primary contributor to intraseasonal SST change in the eastern Pacific, seems to beg the question: what is driving the meridional current? Although the answer to this question is outside the scope of this study and cannot be definitively answered here, the following discussion highlights some preliminary findings. Figure 18 shows an analysis of the currents at the boundaries of the region analyzed in Figure 14. Figure 18 (top) shows the time rate of change of the anomalous mixed layer temperature (blue line) and mixed layer depth (heavy green line) is the climatological response, light green line is total mixed layer depth response) averaged within the region. Figure 18 (middle) shows the anomalous zonal current at  $120^\circ\text{W}$  averaged from  $3^\circ\text{N}$  to  $3^\circ\text{S}$  (light blue line, western boundary of the region), zonal current at  $100^\circ\text{W}$  averaged from  $3^\circ\text{N}$  to  $3^\circ\text{S}$  (red line, eastern boundary), meridional current at  $3^\circ\text{N}$  averaged from  $100^\circ\text{W}$  to  $120^\circ\text{W}$  (green line, northern boundary) and meridional current at  $3^\circ\text{S}$  averaged from  $100^\circ\text{W}$  to  $120^\circ\text{W}$  (dark blue line, southern boundary). The red (blue) asterisks on the abscissa denote the warming (cooling) events used in composite warming (cooling) calculations. During the warming events the meridional current is convergent into the region (on the order of  $4\text{--}5 \text{ cm/s}$ ) and the zonal current is divergent out of the region (on the order of  $-25 \text{ cm/s}$  at the western edge and  $5 \text{ cm/s}$  on the eastern edge). The cooling phase is opposite with meridional currents divergent and zonal current convergent. It is natural to expect that these currents might be driven by the zonal wind via Ekman transport. Figure 18 (bottom) shows zonal wind speed (light blue line, right axis),  $dSST/dt$  (red line),  $du/dx$  (dark blue line), and  $dv/dy$  (green line). Although zonal wind is well correlated and in phase with  $dSST/dt$ , a scale analysis

of the zonal wind speed (approximately  $0.5 \text{ m/s}$ ) shows that the meridional Ekman transport generated at  $3^\circ\text{N}$  and  $3^\circ\text{S}$  would be too small (under  $1 \text{ cm/s}$ ) to drive the  $4\text{--}5 \text{ cm/s}$  meridional current response. Additionally, the zonal current at  $120^\circ\text{W}$  is in opposite phase with the zonal wind implying the presence of remotely forced activity in that region. Zonal and meridional divergence and convergence ( $du/dx$  and  $dv/dy$ , shown in Figure 18 (bottom)) suggests that zonal and meridional transports are on the same order of magnitude. However, the mean meridional temperature gradient in this region is much stronger than the zonal temperature gradient. This would suggest that for equal transport, the meridional advection would have a greater influence on the mixed layer heat budget.

[63] Further study, both in the observational and modeling context, is needed in order to address the uncertainties, the driver of the meridional advection, and the caveats discussed above. In the modeling context, reproducing these results with OGCMs that contain physics other than those in the Gent and Cane model and/or with a coupled ocean-atmosphere model, would be a valuable next step. In the observational context, additional measurements of the zonal and meridional currents need to be made at off-equatorial buoy locations in the eastern Pacific (e.g.,  $2^\circ\text{N}$  and  $2^\circ\text{S}$ ,  $110^\circ\text{W}$  and  $95^\circ\text{W}$ ) for a time period of several years (i.e., several MJO events) to quantify and compare the meridional and zonal advection contributions reported here.

[64] **Acknowledgments.** This work was prepared in conjunction with the first author's dissertation research at State University of New York at Stony Brook. In this regard, the authors would like to thank Dong-Ping Wang, Robert Wilson, and Minghua Zhang for their comments and suggestions on this work. Support for this study was provided under grants NAG5-11033 (D.E.W., L.E.L.) and Salinity, QUICKSCAT, TRMM, and Indian Ocean Biogeochemistry grants (R.M.) as well as the National Science Foundation under grant ATM-0094416 (D.E.W.). This study's analysis and presentation benefited from the use of the NCAR Graphics Package and Seaspace Corporation's TeraScan software system.

## References

- Arakawa, A., and V. R. Lamb (1977), Computational design of the basic dynamical processes of the UCLA general circulation model, in *Methods in Computational Physics*, vol. 17, edited by J. Chang, pp. 173–265, Academic, New York.
- Atlas, R., R. N. Hoffman, S. C. Bloom, J. C. Jusem, and J. Ardizzone (1996), A multiyear global surface wind velocity dataset using SSM/I wind observations, *Bull. Am. Meteorol. Soc.*, **77**, 869–882, doi:10.1175/1520-0477(1996)077<0869:AMGSWV>2.0.CO;2.
- Bentamy, A., Y. Quilfen, F. Gohin, N. Grima, M. Lenaour, and J. Servain (1996), Determination and validation of average wind fields from ERS-1 scatterometer measurements, *Global Atmos. Ocean Syst.*, **4**, 1–29.
- Bishop, J. K. B., W. B. Rossow, and E. G. Dutton (1997), Surface solar irradiance from the International Satellite Cloud Climatology Project 1983–1991, *J. Geophys. Res.*, **102**, 6883–6910.
- Chen, D., L. M. Rothstein, and A. J. Busalacchi (1994), A hybrid vertical mixing scheme and its application to tropical ocean models, *J. Phys. Oceanogr.*, **24**, 2156–2179, doi:10.1175/1520-0485(1994)024<2156:AHVMSA>2.0.CO;2.
- Duchon, C. E. (1979), Lanczos filtering in one and two dimensions, *J. Appl. Meteorol.*, **18**, 1016–1022, doi:10.1175/1520-0450(1979)018<1016:LFIOT>2.0.CO;2.
- Gent, P. R., and M. A. Cane (1989), A reduced gravity, primitive equation model of the upper equatorial ocean, *J. Comput. Phys.*, **81**, 444–480, doi:10.1016/0021-9991(89)90216-7.
- Hayes, S. P., L. J. Mangum, J. Picaut, A. Sumi, and K. Takeuchi (1991), TOGA-TAO: A moored array for real-time measurements in the tropical Pacific Ocean, *Bull. Am. Meteorol. Soc.*, **72**, 339–347, doi:10.1175/1520-0477(1991)072<0339:TTAMAF>2.0.CO;2.



- Hendon, H. H., B. Liebmann, and J. D. Glick (1998), Oceanic Kelvin waves and the Madden-Julian Oscillation, *J. Atmos. Sci.*, **55**, 88–101, doi:10.1175/1520-0469(1998)055<0088:OKWATM>2.0.CO;2.
- Higgins, R. W., and W. Shi (2001), Intercomparison of the principal modes of interannual and intraseasonal variability of the North American monsoon system, *J. Clim.*, **14**, 403–417, doi:10.1175/1520-0442(2001)014<0403:IOTPMO>2.0.CO;2.
- Jones, C. (2000), Occurrence of extreme precipitation events in California and relationships with the Madden-Julian Oscillation, *J. Clim.*, **13**, 3576–3587, doi:10.1175/1520-0442(2000)013<3576:OOEPEI>2.0.CO;2.
- Karnauskas, K. B., R. Murtugudde, and A. J. Busalacchi (2007), The effect of the Galápagos Islands on the equatorial Pacific cold tongue, *J. Phys. Oceanogr.*, **37**, 1266–1281, doi:10.1175/JPO3048.1.
- Kessler, W. S., M. J. McPhaden, and K. M. Weickmann (1995), Forcing of intraseasonal Kelvin waves in the equatorial Pacific, *J. Geophys. Res.*, **100**, 10,613–10,631, doi:10.1029/95JC00382.
- Kraus, E. B., and J. S. Turner (1967), A one-dimensional model of seasonal thermocline. Part II. General theory and its consequences, *Tellus*, **19**, 98–105.
- Lau, K.-M., and P. H. Chen (1986), Aspects of the 40–50 day oscillation during the northern summer as inferred from outgoing longwave radiation, *Mon. Weather Rev.*, **114**, 1354–1367, doi:10.1175/1520-0493(1986)114<1354:AOTDOD>2.0.CO;2.
- Lawrence, D. M., and P. J. Webster (2001), Interannual variations of the intraseasonal oscillation in the South Asian summer monsoon region, *J. Clim.*, **14**, 2910–2922, doi:10.1175/1520-0442(2001)014<2910:IVOTIO>2.0.CO;2.
- Levitus, S., and T. P. Boyer (1994), *World Ocean Atlas 1994*, vol. 4, *Temperature*, NOAA Atlas NESDIS, vol. 4, NOAA, Silver Spring, Md.
- Li, Z. Q., and H. G. Leighton (1993), Global climatologies of solar-radiation budgets at the surface and in the atmosphere from 5 years of ERBE data, *J. Geophys. Res.*, **98**, 4919–4930.
- Liebmann, B., H. H. Hendon, and J. D. Glick (1994), The relationship between tropical cyclones of the western Pacific and Indian oceans and the Madden-Julian Oscillation, *J. Meteorol. Soc. Jpn.*, **72**, 401–412.
- Liebmann, B., G. N. Kiladis, C. S. Vera, A. C. Saulo, and L. M. V. Carvalho (2004), Subseasonal variations of rainfall in South America in the vicinity of the low-level jet east of the Andes and comparison to those in the South Atlantic convergence zone, *J. Clim.*, **17**, 3829–3842, doi:10.1175/1520-0442(2004)017<3829:SVORIS>2.0.CO;2.
- Lorenz, E. N. (1971), N-cycle time-differencing scheme for stepwise numerical integration, *Mon. Weather Rev.*, **99**, 644–648, doi:10.1175/1520-0493(1971)099<0644:ATSFSN>2.3.CO;2.
- Lucas, L. E. (2007), Mechanisms Governing sea surface temperature anomalies in the eastern tropical Pacific Ocean Associated with atmospheric intraseasonal variability, Ph.D. dissertation, 93 pp., State Univ. of N. Y. at Stony Brook, Stony Brook, N. Y.
- Madden, R. A., and P. R. Julian (1971), Detection of a 40–50 day oscillation in the zonal wind in the tropical Pacific, *J. Atmos. Sci.*, **28**, 702–708, doi:10.1175/1520-0469(1971)028<0702:DOADOI>2.0.CO;2.
- Madden, R. A., and P. R. Julian (1994), Observations of the 40–50-day tropical oscillation: A review, *Mon. Weather Rev.*, **122**, 814–837, doi:10.1175/1520-0493(1994)122<0814:OOTDIO>2.0.CO;2.
- Matthews, A. J. (2004), Intraseasonal variability over tropical Africa during northern summer, *J. Clim.*, **17**, 2427–2440, doi:10.1175/1520-0442(2004)017<2427:IVOTAD>2.0.CO;2.
- McPhaden, M. J. (1999), Genesis and evolution of the 1997–98 El Niño, *Science*, **283**, 950–954, doi:10.1126/science.283.5404.950.
- McPhaden, M. J. (2002), Mixed layer temperature balance on intraseasonal timescales in the equatorial Pacific Ocean, *J. Clim.*, **15**, 2632–2647, doi:10.1175/1520-0442(2002)015<2632:MLTBOI>2.0.CO;2.
- McPhaden, M. J., et al. (1998), The Tropical Ocean-Global Atmosphere (TOGA) observing system: A decade of progress, *J. Geophys. Res.*, **103**, 14,169–14,240.
- Murtugudde, R., and A. Busalacchi (1998), Salinity effects in a tropical ocean model, *J. Geophys. Res.*, **103**, 3283–3300, doi:10.1029/97JC02438.
- Murtugudde, R., R. Seager, and A. Busalacchi (1996), Simulation of the tropical oceans with an ocean GCM coupled to an atmospheric mixed-layer model, *J. Clim.*, **9**, 1795–1815, doi:10.1175/1520-0442(1996)009<1795:SOTTOW>2.0.CO;2.
- Murtugudde, R., J. Beauchamp, C. McClain, M. Lewis, and A. Busalacchi (2002), Effects of penetrative radiation on the upper tropical ocean circulation, *J. Clim.*, **15**, 470–486, doi:10.1175/1520-0442(2002)015<0470:EOPROT>2.0.CO;2.
- Price, J. F., R. A. Weller, and R. Pinkel (1986), Diurnal cycling: Observations and models of the upper ocean response to diurnal heating, cooling, and wind mixing, *J. Geophys. Res.*, **91**, 8411–8427, doi:10.1029/JC091iC07p08411.
- Pullen, P. E., R. L. Bernstein, and D. Halpern (1987), Equatorial long-wave characteristics determined from satellite sea surface temperature and in situ data, *J. Geophys. Res.*, **92**, 742–748, doi:10.1029/JC092iC01p00742.
- Reynolds, R. W., and T. M. Smith (1994), Improved global sea surface temperature analyses using optimum interpolation, *J. Clim.*, **7**, 929–948, doi:10.1175/1520-0442(1994)007<0929:IGSSTA>2.0.CO;2.
- Rossow, W. B., and R. A. Schiffer (1991), ISCCP cloud data products, *Bull. Am. Meteorol. Soc.*, **72**, 2–20, doi:10.1175/1520-0477(1991)072<0002:ICDP>2.0.CO;2.
- Seager, R., and M. B. Blumenthal (1994), Modeling tropical Pacific sea-surface temperature with satellite-derived solar radiative forcing, *J. Clim.*, **7**, 1943–1957, doi:10.1175/1520-0442(1994)007<1943:MTPSST>2.0.CO;2.
- Seager, R., M. B. Blumenthal, and Y. Kushnir (1995), An advective atmospheric mixed-layer model for ocean modeling purposes: Global simulation of surface heat fluxes, *J. Clim.*, **8**, 1951–1964, doi:10.1175/1520-0442(1995)008<1951:AAAMLM>2.0.CO;2.
- Shapiro, R. (1970), Smoothing, filtering and boundary effects, *Rev. Geophys. Space Phys.*, **8**, 359–387, doi:10.1029/RG008i002p00359.
- Tian, B. J., D. E. Waliser, R. A. Kahn, Q. B. Li, Y. L. Yung, T. Tyranowski, I. V. Geogdzhavev, M. I. Mishchenko, O. Torres, and A. Smirnov (2008), Does the Madden-Julian Oscillation influence aerosol variability?, *J. Geophys. Res.*, **113**, D12215, doi:10.1029/2007JD009372.
- Waliser, D. E. (2006), Intraseasonal variability, in *The Asian Monsoon*, edited by B. Wang, pp. 203–257, Springer, Heidelberg, Germany.
- Waliser, D. E., R. Murtugudde, and L. E. Lucas (2003), Indo-Pacific Ocean response to atmospheric intraseasonal variability: 1. Austral summer and the Madden-Julian Oscillation, *J. Geophys. Res.*, **108**(C5), 3160, doi:10.1029/2002JC001620.
- Wang, B., and H. Rui (1990), Synoptic climatology of transient tropical intraseasonal convection anomalies: 1975–1985, *Meteorol. Atmos. Phys.*, **44**, 43–61, doi:10.1007/BF01026810.
- Weickmann, K. M. (1991), El Niño–Southern oscillation and Madden-Julian (30–60 day) oscillations during 1981–1982, *J. Geophys. Res.*, **96**, 3187–3195.
- Xie, P. P., and P. A. Arkin (1997), Global precipitation: A 17-year monthly analysis based on gauge observations, satellite estimates, and numerical model outputs, *Bull. Am. Meteorol. Soc.*, **78**, 2539–2558, doi:10.1175/1520-0477(1997)078<2539:GPAYMA>2.0.CO;2.
- Yasunari, T. (1979), Cloudiness fluctuations associated with the Northern Hemisphere summer monsoon, *J. Meteorol. Soc. Jpn.*, **57**, 227–242.
- Zhang, C. (2001), Intraseasonal perturbations in sea surface temperatures of the equatorial eastern Pacific and their association with the Madden-Julian Oscillation, *J. Clim.*, **14**, 1309–1322, doi:10.1175/1520-0442(2001)014<1309:IPISST>2.0.CO;2.
- Zheng, Y., D. E. Waliser, W. Stern, and C. Jones (2004), The role of coupled sea surface temperatures in the simulation of the tropical intraseasonal oscillation, *J. Clim.*, **17**, 4109–4134, doi:10.1175/JCLI3202.1.

L. E. Lucas, Climate Program Office, NOAA, 1315 East-West Hwy., Room 12712, Silver Spring, MD 20910, USA. (sandy.lucas@noaa.gov)

R. Murtugudde, Earth System Science Interdisciplinary Center, University of Maryland, 5825 University Research Ct., Suite 4001, College Park, MD 20740-3823, USA.

D. E. Waliser, Water and Carbon Cycles Group, Jet Propulsion Laboratory, 4800 Oak Grove Dr., Pasadena, CA 91109, USA.